JOURNAL OF GEOPHYSICAL RESEARCH, VOL. 111, B08304, doi:10.1029/2005JB003872, 2006

Stability regimes of a dilatant, fluid-infiltrated fault plane in a three-dimensional elastic solid

G. Hillers[1,2] and S. A. Miller[1,3]

Received 7 June 2005; revised 7 April 2006; accepted 4 May 2006; published 17 August 2006.

[1] We investigate in a systematic parameter space study dilatant effects on slip evolution of a fluid-infiltrated fault in the continuum limit. The fault is governed by rate- and state-dependent friction and an empirical law for porosity evolution. We focus on the response of systems as a function of fluid-related parameters, such as the degree of overpressurization, dilatancy and diffusivity. This study emphasizes the exploration of the parameter space for homogeneous along-strike properties to investigate the evolution of spatiotemporal slip depending on hydromechanical processes. Three types of responses emerge. First, system-wide unstable stick-slip develops for drained conditions, and for undrained conditions if mechanisms leading to an increase in pore space are less effective. The critical stiffness depends on hydraulic diffusivity and dilatancy, which is shown to correspond with interevent times of simulated stick-slip events. During instabilities the evolution of hydraulic variables differ significantly between drained and undrained conditions. Second, stable creep is a result of dilatant processes. Third, systems situated in transitional stability regimes develop nonuniform slip pattern in space and time, revealing a possible explanation for rupture termination and observed stable afterslip. Although these patterns are produced by models located in transition zones of the parameter space, the occurrence of heterogeneous slip evolution is persistent for an extensive range of parameter values. Since transition zones contain an broad range of plausible conditions in the crust, they do not represent extreme cases.

Citation: Hillers, G., and S. A. Miller (2006), Stability regimes of a dilatant, fluid-infiltrated fault plane in a three-dimensional elastic solid, *J. Geophys. Res.*, *111*, B08304, doi:10.1029/2005JB003872.

1. Introduction

[2] The role of fluids is well established as very important in the earthquake process but not well understood. Observational, laboratory, and numerical studies suggest that fluid related processes are responsible for a wide range of phenomena related to faulting. Examples of fluid-driven aftershocks [*Nur and Booker*, 1972; *Bosl and Nur*, 2002; *Miller et al.*, 2004; *Piombo et al.*, 2005, and references therein] reveal the importance of fluid flow in the crust associated with main shocks. Migration and redistribution of fluids is also reported to trigger earthquake swarms [*Waite and Smith*, 2002]. Remotely triggered earthquakes occur preferentially in geothermal and volcanic areas, suggesting that fluids are important in explaining this type of seismic activity [*Hill et al.*, 1993; *Husen et al.*, 2004]. Another detected phenomenon stressing the mechanical importance in earthquake nucleation are elevated fluid pressures at the hypocenter region of the *M* 7.2 1995 Kobe earthquake, Japan [*Zhao et al.*, 1996]. Compartmentalized high fluid pressures [*Byerlee*, 1993] are supported in part by seismic and drilling experiments along a decollement near Barbados [*Moore et al.*, 1995; *Fisher and Zwart*, 1996]. Field evidence implies the formation and destruction of low permeability/diffusivity seals to drive pore pressure in excess of hydrostatic [*Sibson*, 1994]. Laboratory experiments [*Sleep and Blanpied*, 1992; *Blanpied et al.*, 1998a; *Lockner and Byerlee*, 1994] unveil mechanisms responsible for the development of overpressured pore fluid states that might act as nucleation mechanisms for earthquakes, leading to a fault valve behavior [*Sibson*, 1992; *Cox*, 1995]. Three important mechanisms of porosity reduction have been identified: (1) Plastic pore closure due to ductile creep [*Sleep*, 1995], which is applied in the present study; (2) stress induced dissolution and redeposition in pores; and (3) crack healing and sealing, i.e., local redistribution of solid material [*Walder and Nur*, 1984; *Nur and Walder*, 1992]. *Moore et al.* [1994] investigated a corrosive effect of high pressure/temperature conditions leading to formation of impermeable seals that effectively trap pore fluids in the fault zone, which is a fundamental premise to explain mechanical properties of weak fault zones [*Rice*, 1992; *Faulkner and Rutter*, 2001]. Existing fluids, their migration and related poroelastic effects alter stress states in the crust and are thus an important trigger mechanism for earthquakes [*Byerlee*, 1993, 1990; *Beeler et al.*, 2000; *Cocco and Rice*, 2002].

[1] Institute of Geophysics, ETH Honggerberg, Zurich, Switzerland.
[2] Now at the Institute for Crustal Studies, University of California, Santa Barbara, California, USA.
[3] Now at the Department of Geodynamics and Geophysics, University of Bonn, Bonn, Germany.

0148-0227/06/2005JB003872$09.00

[3] Several numerical studies [*Lockner and Byerlee*, 1995; *Segall and Rice*, 1995; *Miller et al.*, 1996; *Sleep*, 1997; *Taylor and Rice*, 1998; *Miller et al.*, 1999; *Chambon and Rudnicki*, 2001; *Fitzenz and Miller*, 2001] outlined principal mechanical implications of crustal pore pressure regimes in excess of hydrostatic. To pursue previous work, we focus on the role of dilatancy in active faulting [*Lockner and Byerlee*, 1994; *Rudnicki and Chen*, 1988; *Chambon and Rudnicki*, 2001] and investigate effects of hydromechanical properties on spatiotemporal slip evolution of a two-dimensional (2-D) vertical strike-slip fault plane embedded in a homogeneous half-space. More specifically, we apply the formalism of a single degree of freedom elastohydraulic model developed by *Segall and Rice* [1995] to the geometry of an extended 2-D fault plane used by *Rice* [1993] and in other purely elastic models [*Tse and Rice*, 1986; *Ben-Zion and Rice*, 1995, 1997; *Rice and Ben-Zion*, 1996]. Hence the present study expands ideas from existing 1-D, 2-D, and 3-D faulting models. The simulated evolution of seismicity depends on fluid related processes in response to pore space compacting mechanisms on a two-dimensional plane [e.g., *Lockner and Byerlee*, 1995; *Miller et al.*, 1996, 1999]. In contrast to previous elastohydraulic studies we solve governing equations in the continuum limit. Therefore results presented here are not dominated by the spatial discretization of the model space. Although the model design allows investigations of natural likely heterogeneous parameter distributions we apply only homogeneous parameter distributions along strike. Heterogeneous distributions of hydraulically important quantities are explored by *Hillers and Miller* [2006].

[4] We perform numerical experiments to simulate slip evolution of fault zones in response to different degrees of hydraulic connectivity to the surrounding pore pressure regime. Physical evidence for high diffusivities between fault zone and surrounding medium at all stages of the seismic cycle originate in fracture related flow paths. Contrary, experimental results indicate the formation of low-permeability seals between fault gouge and the country rock. The fault may remain sealed indefinitely even though it may experience continuous creep or earthquakes [*Blanpied et al.*, 1992]. As a consequence, diffusivity has been shown to vary over several orders of magnitude [*Caine et al.*, 1996; *Faulkner and Rutter*, 2001], even along a single fault structure such as the Median Tectonic Line, Japan [*Wibberly and Shimamoto*, 2003]. To incorporate this knowledge about naturally occurring ranges in permeability, we make significant approximations in the formation and maintenance of hydraulically isolated fault planes, but we demonstrated that these approximations have substantial supporting evidence. As worked out by *Taylor and Rice* [1998] analytically, stabilizing dilatant strengthening effects occurring in an overpressured fault might be counteracted by an expansion of pore fluids by shear heating. To limit the present study, we do not incorporate temperature-dependent processes so that possible further weakening mechanisms are not considered here.

[5] The paper is organized as follows. First, we outline the conceptual model which then is translated into its numerical representation. We introduce the governing equations for friction, pore pressure and porosity evolution necessary to simulate processes of interest by emphasizing their application to the extended 2-D planar fault. We then discuss a typical model implementation to illustrate the effect of hydraulic parameters on the continuum limit approach. Some constant parameter settings will be introduced before we present theoretically derived stability regimes. Main results will be discussed within the framework of these regimes, starting with comparisons of end-member cases to published results. The evaluation of model responses in transition zones is given in section 2, in which we analyze the effect of diffusivity on interevent times before we focus on dilatancy related processes. Before we conclude, obtained results will be compared to existing models and viewpoints.

2. Conceptual Model

[6] The conceptual model is an extension of the models discussed by *Rice* [1993] and *Segall and Rice* [1995] to a fluid-infiltrated two-dimensional vertical strike-slip fault plane embedded in an infinite elastic half-space with rigidity $G = 30$ GPa and shear wave velocity $v_s = 3$ km s^{-1}. The fault is governed by rate- and state-dependent friction, dilatancy, and pore compacting mechanisms. Slip u is calculated in the uppermost 24 km of the fault which is driven by aseismic plate movement of $v^{\infty} = 35$ mm yr^{-1} at its downward extension (Figure 1 and notation section). Pressure p of fluids filling the open pore space ϕ in the fault zone is connected via effective diffusivity c^* to the pore pressure regime in the surrounding medium, p^{∞}. Both pressure regimes are assumed to equilibrate over an implicit length scale L_D, which can be interpreted as the thickness of the fault bounding walls or connected damage zone.

[7] Hydraulic diffusivity is assumed to be constant and homogeneous across the fault plane, i.e., permeability is invariant throughout the seismic cycle. Possible changes in hydraulic diffusivity during slip episodes because of temperature and normal stress changes are ignored. Experimental [*Zhang and Tullis*, 1998; *Zhang et al.*, 1999, 2001] and field studies [*Sibson and Rowland*, 2003] reveal a highly anisotropic permeability structure of fault zones with higher fluid flow inside the fault than perpendicular to the fault walls, leading to the formation of a conduit in the fault core. As demonstrated by *Yamashita* [1998], the expected fluid migration has important implications on the fault's seismogenesis. However, the focus of this study is the impact of certain permeability regimes in the fault bounding rocks on slip evolution. We thus follow a simplified approach by neglecting possible fluid flow in the fault zone. Pore pressure redistribution is a function of connectivity to the pressure state in the host rock under sufficiently drained conditions. The importance of hydraulic parameters on seismicity are demonstrated in the analysis of a lumped parameter model, where differences of responses between effectively drained and undrained models were investigated [*Segall and Rice*, 1995].

[8] If a fault or part of a fault is overpressured, it must be continuously supplied with a fluid pressure source if the overpressure is to be maintained, otherwise pore pressure regimes will equilibrate for $c^* > 0$ yr^{-1}. Possible pressure sources are a direct fluid source at depth, dehydration, or the reduction of the available pore space [*Miller et al.*, 1999]. We adopt the compaction formalism derived by *Segall and*

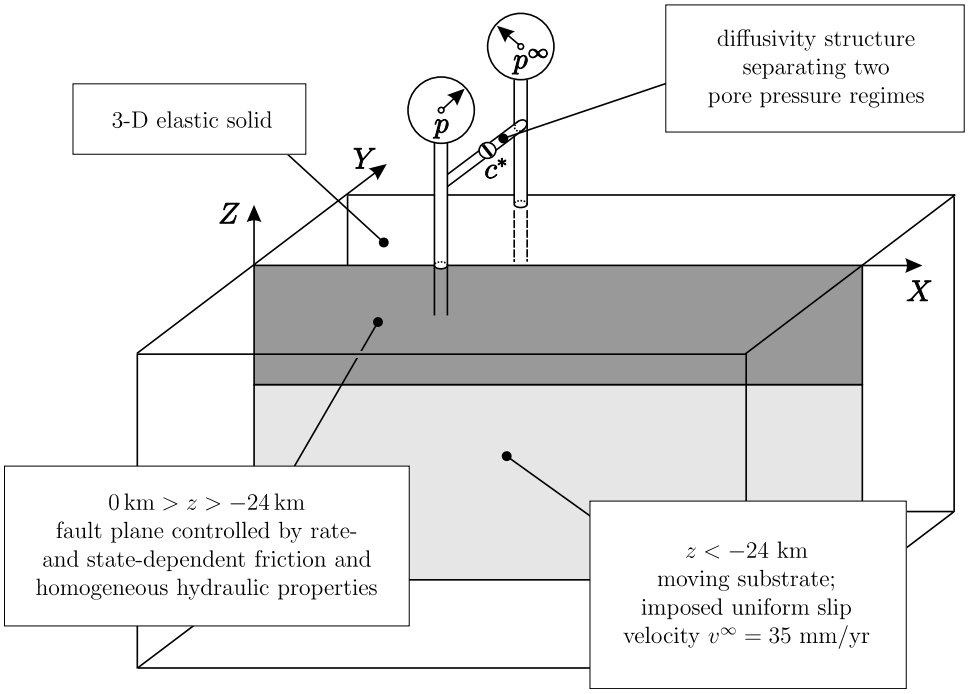

Figure 1. The 2-D vertical strike-slip model fault plane embedded in a 3-D elastic half-space. The fault's response is governed by rate-and-state friction and an empirical law for pore compaction. We use homogeneous hydromechanical properties along strike. The fault is loaded by aseismic slip rate, v^∞, at its downward extension (light grey area). Pore pressure in the fault, p, is connected via effective hydraulic diffusivity, c^*, to the pore pressure state in the crust, p^∞. Slip is calculated over a depth range of $Z_{\text{depth}} = -24$ km, where governing equations apply (dark grey area). The periodic repeat distance along strike is $X_{\text{length}} = 100$ km, unless stated otherwise.

Rice [1995] to fit data obtained in drained experiments by *Marone et al.* [1990], noticing that this particular dilatancy constitutive law has been shown to produce only small increases in fault zone pore pressure. The present model allows the investigation of the long-term seismic response to external loading over several cycles, and a qualitative analysis of specific slip events. We focus on the effect of different fluid-related parameters on spatiotemporal slip evolution. These parameters are the effective hydraulic diffusivity, c^*, a dilatancy coefficient, ε, and the degree of overpressurization, $\lambda = p/\sigma_n$, where the normal stress σ_n is assumed to be lithostatic. A translation of the conceptual model into numerical tractable evolutionary equations for shear stress τ, state θ, slip velocity v, pore pressure p and porosity ϕ is derived in section 3.

3. Numerical Model

3.1. Stress-Slip Relation

[9] Figure 1 shows the model geometry and coordinate system of a vertical strike-slip fault plane in a 3-D elastic medium following *Rice* [1993], *Ben-Zion and Rice* [1995, 1997], and *Lapusta et al.* [2000]. The evolution of slip, $u(x, z, t)$, on the fault plane $y = 0$ is associated with a redistribution of shear stress, $\tau(x, z, t)$. In the discretized case, the resulting integral relation connecting u and τ can be expressed by a set of linear equations based on the quasi-static elastic solution for uniform slip over a rectangular dislocation cell in an elastic half-space [*Chinnery*, 1963]

$$\tau_{ij}(t) = \tau^0 + \tau^{\text{r}}_{ij}(t) - v_{ij}(t)\,\eta_0. \tag{1}$$

[10] Here, τ^0 is a background stress value chosen to keep $\tau_{ij} > 0$ in cases where slip is possibly overshooting, but τ^0 has no influence on the evolution of the system. Shear stress redistribution due to loading and slip on the fault is denoted by $\tau^{\text{r}}_{ij}(t) = \Sigma_k \Sigma_l K_{|i-k|,j,l}(v^\infty\ t - u_{kl}(t))$. Indices i, k and j, l denote cell locations on the numerical grid along strike and depth, respectively. The elastostatic kernel (or stiffness matrix) K relates the slip at cell kl, u_{kl}, to change of stress at cell ij, τ_{ij}, at some time t, and was calculated assuming 10 periodic repetitions of the fault along strike to approximate infinite periodic boundary conditions. A constant driving plate velocity, v^∞, is imposed at the downward extension of the fault and $\dot{u}_{ij}(t) = v_{ij}(t)$ is the slip rate of a certain cell. The term η_0 in equation (1) accounts for seismic radiation damping and is equal to $G/(2v_s)$ [*Rice*, 1993]. Including this factor makes the description quasi-dynamic, since it incorporates the elastodynamic limit result for any instantaneous changes in $\tau_{ij}(t)$ and $v_{ij}(t)$. It also has the advantage of allowing stable calculations to be carried through dynamic instabilities, without requiring the computationally expensive calculations of the exact elastodynamic solution performed by *Ben-Zion and Rice* [1997], *Lapusta et al.* [2000], and *Lapusta and Rice* [2003].

3.2. Friction

[11] To describe the frictional resistance of two adjacent fault walls, we use the laboratory derived rate- and state-

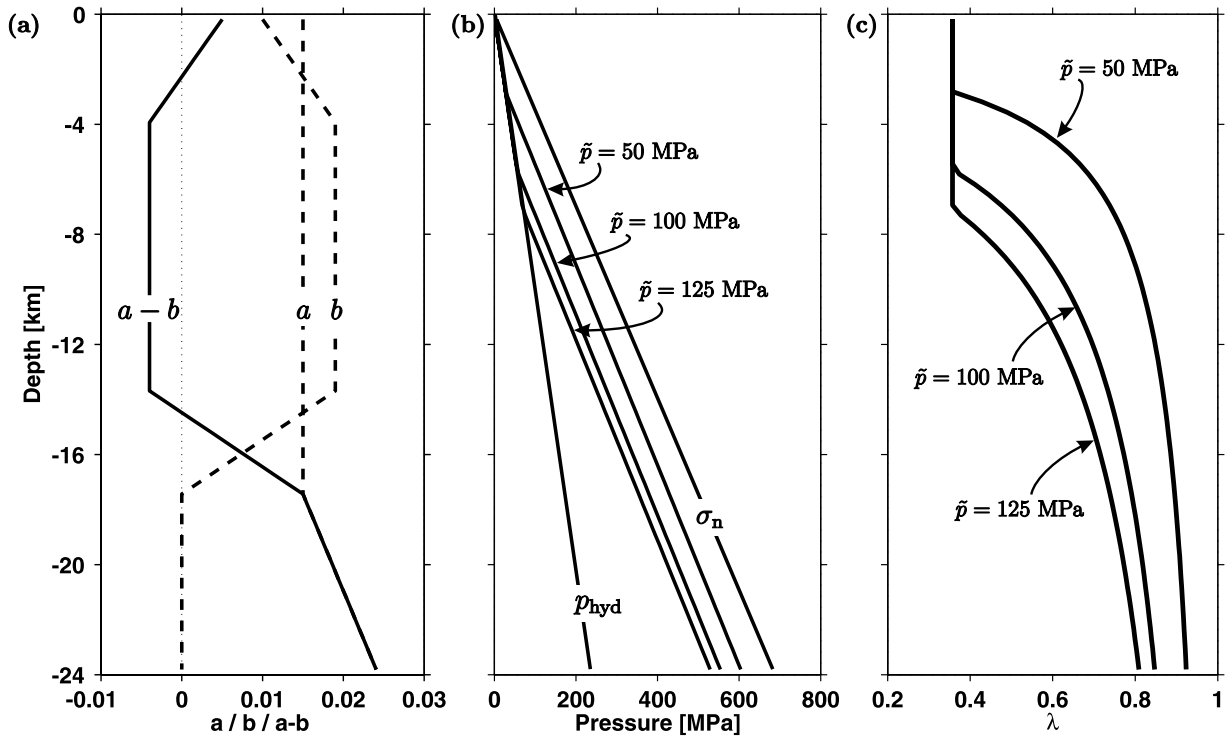

Figure 2. Depth dependence of relevant parameters used in the simulations. (a) Frictional scaling parameters a, b, and $a - b$. (b) Lithostatic normal stress, σ_n, hydrostatic gradient, p_{hyd}, and pore pressure profiles obtained for $\tilde{p}$ = [50, 100, 125] MPa, respectively, using $p(z)$ = max [$p_{hyd}(z)$, $\sigma_n(z) - \tilde{p}$]. (c) Corresponding $\lambda = p/\sigma_n$ profiles.

dependent friction formulation. We apply the standard Dieterich-Ruina description of the friction coefficient, $\mu(x, z, t)$ [*Dieterich*, 1979; *Ruina*, 1983], which depends on sliding velocity, $v(x, z, t)$, and a state variable, $\theta(x, z, t)$,

$$\mu(x,z,t) = \mu_0 + a(z)\ln\left(\frac{v(x,z,t)}{v_0}\right) + b(z)\ln\left(\frac{v_0\,\theta(x,z,t)}{L}\right). \quad (2)$$

The state variable is interpreted as a measure of maturity of contacts on a fault surface. For the Dieterich-Ruina ("slowness" or "ageing") form of the law, the state variable evolves according to

$$\frac{\partial\theta(x,z,t)}{\partial t} = 1 - \frac{v(x,z,t)\,\theta(x,z,t)}{L}. \quad (3)$$

In equation (2), μ_0 is the nominal friction, a and b are temperature and hence depth-dependent frictional scaling parameters (Figure 2a), L is a critical slip distance, and $v_0 = v^{\infty}$ is a normalizing constant. The characteristic slip distance L is interpreted as a length scale over which a new population of contacts between two surfaces evolves. Laboratory values of L depend on the fault roughness and gouge width [*Marone et al.*, 1990]. Typical values in rock sliding experiments done to date are in the range 10^{-6} m to 5×10^{-4} m [*Ben-Zion*, 2003]. The size of L determines a critical spatial dimension of a process or nucleation zone, h^* [*Dieterich*, 1992; *Rice*, 1993; *Rubin and Ampuero*, 2005], and to solve the problem in the continuum limit it is necessary to use $h \ll h^*$, where h is the numerical cell size [*Rice*, 1993]. This places strong constraints on the computational efficiency, since cpu time scales with the number of cells. Thus calculating slip histories within the continuum framework can be done at present only for some scaled up versions of laboratory values of L. The coefficient of friction, μ, relates the shear stress on a fault, τ, to the effective normal stress (Figure 2b), $\sigma_e = \sigma_n - p$, via

$$\tau(x,z,t) = \mu(x,z,t)\,(\sigma_n(z) - p(x,z,t)), \quad (4)$$

Inserting equation (2) into equation (4) and differentiating the resulting equation of motion with respect to time leads to the time-dependent velocity evolution

$$\frac{\partial v(x,z,t)}{\partial t} = \left(\frac{\eta}{\sigma_e(x,z,t)} + \frac{a(z)}{v(x,z,t)}\right)^{-1} \cdot \left(\frac{\dot{\tau}^r(x,z,t) + \mu(x,z,t)\,\dot{p}(x,z,t)}{\sigma_e(x,z,t)} - \frac{b(z)\,\dot{\theta}(x,z,t)}{\theta(x,z,t)}\right), \quad (5)$$

where overdots denote time derivatives. We use the effective damping parameter $\eta = f_\eta \times \eta_0$, with f_η being some factor controlling quasi-dynamic ($f_\eta = 1$) or over-damped quasi-dynamic ($f_\eta \gg 1$) simulations. For consequences on slip evolution with $f_\eta \gg 1$ see *Rice* [1993]. Temporal changes in shear stress, $\dot{\tau}^r$, are given by the sum over velocity differences, multiplied by the stiffness kernel from equation (1), state evolution $\dot{\theta}$ is described by equation (3) and hydraulic properties $\dot{p}$ and $\dot{\phi}$ evolve in a way now described.

3.3. Pore Pressure Redistribution

[12] We refrain from reevaluating the derivation leading to the applied constitutive law of pore pressure and porosity

evolution developed by *Segall and Rice* [1995]. Instead, we outline the main assumptions and rewrite the resulting equations in the framework of the present coordinate system. A scalar specific discharge per unit area, q, can be related to pore pressure gradient causing flow via Darcy's law

$$q = -\rho_f \frac{\kappa}{\nu} \frac{\partial p(x,y,z,t)}{\partial y}, \tag{6}$$

where ρ_f is the fluid density, ν the dynamic pore fluid viscosity and κ is the scalar permeability (i.e., the ability of the rock to transmit fluid through its connected pore space, ϕ). Continuity of fluid mass per unit volume $m = \phi\rho_f$ is required, and by distinguishing between elastic and plastic pore deformation the resulting change in porosity can be written as the sum of an elastic and plastic (denoted by $\dot{\phi}(x, z, t)$) component. Currently, we ignore possible shear heating effects [*Blanpied et al.*, 1998b] on pore pressure change, which could counteract rapid sliding induced compressibility of the pore fluid by its thermal expansion [*Taylor and Rice*, 1998; *Andrews*, 2002; *Garagash and Rudnicki*, 2003a, 2003b]. The irreversible porosity reduction acts as a direct source term in the diffusion equation

$$\frac{\partial p(x,y,z,t)}{\partial t} = c \frac{\partial^2 p(x,y,z,t)}{\partial y^2} - \frac{\dot{\phi}(x,z,t)}{\beta}, \tag{7}$$

where β is the porosity times the sum of fluid and elastic pore compressibility, respectively. Although β is a function of the evolving pore space, ϕ, we follow *Segall and Rice* [1995] and *Taylor and Rice* [1998] and use $\beta = 5 \times 10^{-4}$ MPa^{-1} = const in our numerical experiments. This value has been obtained by *Segall and Rice* [1995], choosing $\phi = 0.05$ = const from an interpretation of data by *Marone et al.* [1990]. We use 10^{-2} MPa^{-1} for the elastic pore compressibility after *David et al.* [1994], and 5×10^{-4} MPa^{-1} for the fluid compressibility. The parameter $c = \kappa(\nu\beta)^{-1}$ denotes hydraulic diffusivity. It has the unit $[L^2T^{-1}]$ and is thus the inverse of that amount of time over which two pressure regimes, p and p^∞, separated by a medium with property c, will be equilibrated. This medium is assumed to have a certain spatial dimension and thus a characteristic diffusion length, L_D. Physically it can be interpreted as being a cemented border bounding an active fault zone with lower permeability than either the fault or the surrounding rock mass. Implicitly assuming this length scale, the effective hydraulic diffusivity scales to $c^* = c/L_D^2$. We consider potential fluid flow only in the y dimension perpendicular to the fault, which simplifies $\partial^2 p(x, y, z, t)/\partial y^2$ to $(p^\infty(z) - p(x, z, t))/L_D^2$. Using effective diffusivity [*Segall and Rice*, 1995], equation (7) can thus be written as

$$\frac{\partial p(x,z,t)}{\partial t} = c^*(p^\infty(z) - p(x,z,t)) - \frac{\dot{\phi}(x,z,t)}{\beta}. \tag{8}$$

In the following analysis we focus on the difference in slip evolution between drained ($c^* \to \infty$) and undrained faults ($c^* \to 0$).

3.4. Porosity Evolution

[13] The derivation of the constitutive law for plastic porosity changes is based on laboratory experiments by *Marone et al.* [1990] and *Lockner and Byerlee* [1994]. They performed velocity stepping experiments in which the porosity changes were measured under nominally drained ($\dot{p} = 0$) conditions. *Segall and Rice* [1995] interpreted these observations from the viewpoint of the steady state concept in soil mechanics. At constant slip speed the porosity ϕ evolves over the same length scale, L, as the state variable θ toward a steady state value ϕ_{ss}

$$\frac{\partial \phi(x,z,t)}{\partial t} = -\frac{v(x,z,t)}{L}(\phi(x,z,t) - \phi_{ss}(x,z,t)), \tag{9}$$

where ϕ_{ss} follows

$$\phi_{ss}(x,z,t) = \phi_0 + \varepsilon \ln\left(\frac{v(x,z,t)}{v_0}\right) \tag{10}$$

and ϕ_0 and ε denote a reference porosity and the dilatancy coefficient, respectively.

[14] The system's response is thus governed by five interdependent first-order ordinary differential equations in the five parameters friction μ, state variable θ, slip rate v, pore pressure p and porosity ϕ

$$\begin{aligned}
\dot{\mu} &= \dot{\mu}\left(v, \theta, \dot{v}, \dot{\theta}\right) \\
\dot{\theta} &= \dot{\theta}\left(v, \theta\right) \\
\dot{v} &= \dot{v}\left(v, \theta, p, \mu, \dot{p}, \dot{\theta}, \dot{\tau}^r\right) \\
\dot{p} &= \dot{p}\left(p, \dot{\phi}\right) \\
\dot{\phi} &= \dot{\phi}\left(v, \phi\right).
\end{aligned} \tag{11}$$

3.5. Computation Technique

[15] We solve the set of six resulting first-order ordinary differential equations (equation (11) plus $\dot{u} = v$) using an implicit Runge-Kutta (RK) method for stiff systems with adaptive step size control, RADAU5, by *Hairer and Wanner* [1996]. The present geometry allows the use of the fast Fourier transform (FFT) to calculate the along-strike contribution of the stress redistribution, τ^r, executing a matrix multiplication including the stiffness kernel K [*Rice*, 1993; *Stuart and Tullis*, 1995; *Rice and Ben-Zion*, 1996]. Details of the numerical procedure and specific numerical parameter choices can be found in the appendix of *Hillers* [2006]. Certain simulations developing high slip velocities (10^8 m yr^{-1}) during system-wide instabilities with $f_\eta = 1$ took up to 10 days of cpu time on a Compaq TruUnix 700 MHz machine, due to the computationally expensive implicit RK scheme.

4. Model Implementation

[16] To ensure that simulated slip evolutions are independent of the spatial discretization of the numerical grid, the condition $h \ll h^*$ must hold to solve the governing equations in the continuum limit [*Rice*, 1993]. Here, h^* is a critical cell size that is related to the self-stiffness of the most critical cell in the grid, k^{cr}. For the current elastohydraulic problem the general critical stiffness has been derived to [*Segall and Rice*, 1995; *Taylor and Rice*, 1998]

$$k^{cr} = \frac{1}{L}\left[\sigma_e(b-a) - \frac{\varepsilon\mu_0}{\beta}F(c^*)\right], \tag{12}$$

Table 1. Overview of the Models Discussed in Figure 8[a]

Model	ε	$\tilde{p}$, MPa	$\varepsilon_{\tilde{p}}^{+}$	L, m	h_u^*, km	h/h_u^*	Response	Figure
U1	2×10^{-5}			0.03	3.33	0.12	unstable stick-slip	
P1	5×10^{-5}			0.015	2.20	0.18	pattern	9a, 9d, 12d
O1	8×10^{-5}			0.015	3.26	0.12	oscillations	
S1	10^{-4}	50	1.4×10^{-4}	0.03	9.54	0.04	stable sliding	12h
S1	10^{-4}			0.015	4.77	0.08	different L, same response	
S2	10^{-3}			0.03	<0	<0	stable sliding ($\varepsilon > \varepsilon_{50}^{+}$)	
U2	2×10^{-5}			0.03	1.54	0.25	unstable stick-slip	
P2	5×10^{-5}			0.06	3.74	0.11	pattern	
P3	7×10^{-5}			0.03	1.90	0.21	pattern	9c, 9f, 12f
P4	10^{-4}	100	2.8×10^{-4}	0.03	2.20	0.18	pattern	9b, 9e, 10, 12e
S3	2×10^{-4}			0.03	4.77	0.08	stable sliding	
S4	3×10^{-4}			0.03	<0	<0	stable sliding ($\varepsilon > \varepsilon_{100}^{+}$)	
S6	10^{-3}			0.02	<0	<0	stable sliding ($\varepsilon > \varepsilon_{100}^{+}$)	
U3	2×10^{-5}			0.03	1.22	0.32	unstable stick-slip	
U4	10^{-4}			0.08	4.24	0.09	unstable stick-slip	
O2	2×10^{-4}	125	3.6×10^{-4}	0.03	2.60	0.15	oscillations	11, 12g
S5	5×10^{-4}			0.03	<0	<0	stable sliding ($\varepsilon > \varepsilon_{125}^{+}$)	

[a]For all simulations $c_u^* = 10^{-4}$ yr^{-1}, $X_{\text{length}} = 100$ km, $nx = 256$. All experiments were performed with $f_\eta = 10^4$ and $f_\eta = 1$. Remarks to response types correspond to both realizations, confirming the validity of results for variable degrees of damping. For differences in details of slip evolutions between simulations with $f_\eta = 10^4$ and $f_\eta = 1$, see text and Figure 9.

where $F(c^*)$ varies nonlinearly between 0 (for $c^* \to \infty$) and 1 (for $c^* \to 0$). In the former, drained (d), case k^{cr} approaches the value for purely elastic problems obtained by *Ruina* [1983], *Rice and Ruina* [1983], and *Gu et al.* [1984], $k_d^{\text{cr}} = \sigma_e(b - a)/L$. Hence, in the drained limit, the critical cell size h_d^* becomes [*Rice*, 1993]

$$h_d^* = \frac{2GL}{\pi \sigma_e (b-a)_{\max}}. \tag{13}$$

In the latter, undrained (u), case the critical spring stiffness k_u^{cr} is a function of $\varepsilon\mu_0/\beta$, making it thus sensitive to porosity controlling parameters

$$k_u^{\text{cr}} = \frac{1}{L}\left[\sigma_e(b-a) - \frac{\varepsilon\mu_0}{\beta}\right]. \tag{14}$$

Following the line of argument for the derivation of h_d^*, the critical cell size for undrained conditions h_u^* has been found to [*Taylor and Rice*, 1998]

$$h_u^* = 2GL\left[\pi\left(\sigma_e(b-a)_{\max} - \frac{\varepsilon\mu_0}{\beta}\right)\right]^{-1}. \tag{15}$$

Now that two critical cell sizes h_u^* and h_d^* exist for the undrained and drained limit, respectively, their relative value has to be determined to fulfill the continuum limit restriction $h \ll \min[h_u^*, h_d^*]$. On the basis of the examination of the denominator of equation (15), *Taylor and Rice* [1998] deduced that in regions where h_u^* is positive, h_d^* will always be smaller of the two possible critical cell sizes. Thus $h_u^* \geq h_d^*$ always holds true and the requirement $h \ll h^*$ approaches $h \ll h_d^*$.

[17] Beyond its numerical importance, h^* is found to have a physical interpretation in that it determines the nucleation size of model earthquakes [*Dieterich*, 1992; *Lapusta et al.*, 2000; *Rubin and Ampuero*, 2005]. Equation (15) reveals that any choice for L has a direct effect on the smallest earthquake which can be generated by a model with a given spatial discretization. With the experimentally derived values for L cited above in the submillimeter range, the cell size of the grid must be on the order of a meter, resulting in a numerically intractable large model space. This forces us to use L values in the centimeter range. In the present study the typical size of a computational cell is 390 m and we use values between $L = 0.015$ m and $L = 0.08$ m. Together with variable values determining h^*, h/h_d^* is maximum 0.27 and h/h_u^* exceeds 0.3 only in one case (Table 1), whereas for certain simulations h/h_u^* is as small as 0.09. These values raise the question whether we treat the problem properly in the continuum limit defined by *Rice* [1993]. There, the required spatial resolution is met by a ratio of $h/h^* = 0.25$, which has also been used in the 2-D dip-slip model of *Taylor and Rice* [1998], whereas *Ben-Zion and Rice* [1995] used $h/h^* = 0.13$ in their 3-D strike-slip continuum realization. Furthermore, *Kato and Hirasawa* [1997, 1999] performed 2-D subduction simulations with a ratio of $h/h^* = 0.06$, and *Hirose and Hirahara* [2002] and *Shibazaki and Iio* [2003] used $h/h^* = 0.29$ and $h/h^* = 0.6$ in a 3-D subduction model, respectively, being confident to produce no numerical artifacts. Note that *Lapusta et al.* [2000], who solved the full elastodynamic problem in a 2-D implementation on a strike-slip fault geometry, had to reach a minimum ratio of $h/h^* = 0.025$ to produce grid-independent results. However, our execution of the quasi-dynamic approach is designed to investigate qualitatively the long term evolution of drained or undrained fault zones, and thus we do not focus on a high-resolution study in the line of *Lapusta et al.* [2000]. The comparison to other studies suggests we meet the requirement formulated by *Rice* [1993] and applied by *Hirose and Hirahara* [2002]. However, we cannot prove to obtain the "true" model response in the sense of *Lapusta et al.* [2000], where any increase in resolution does not affect the system's response.

5. Parameter Setting

[18] We use the depth distribution of frictional scaling parameters a and b obtained by *Blanpied et al.* [1991] (Figure 2a), indicating a velocity-strengthening ($a > b$) zone

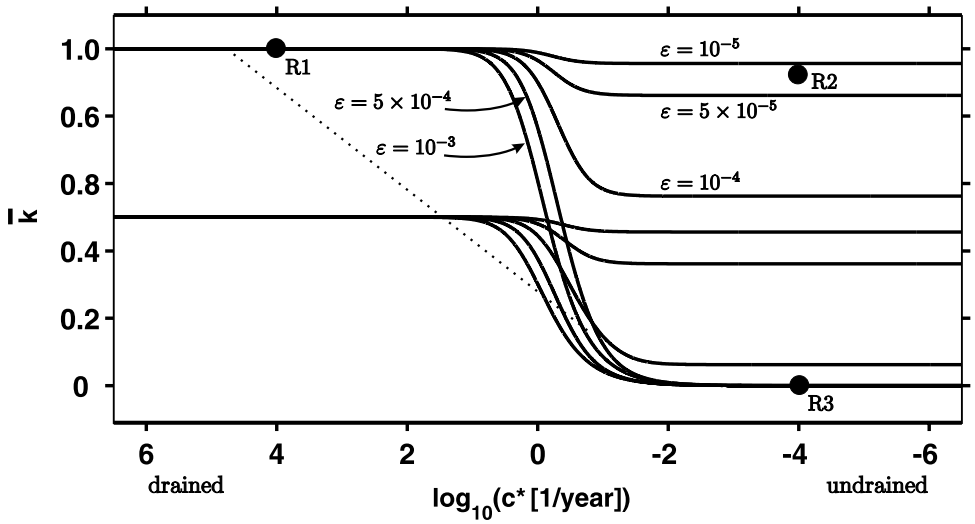

Figure 3. Graphical representation of equation (12). Normalized stiffness, $\bar{k} = k^{cr}/k_d^{cr}$ for a given set of a, b values, as a function of effective diffusivity, c^*. Two sets of lines correspond to different values of b, with $a = 0.015 = \text{const}$, $\sigma_e = 200$ MPa. Top set is for $b = 0.019$; middle set is for $b = 0.017$. For $a > b$, the response is always stable (k^{cr} is not defined), whereas $a < b$ allows for stable as well as unstable slip rates, depending on c^* and on the efficiency of dilatant processes, i.e., on the relative size of $\varepsilon\mu_0/\beta$. The dotted line approximates the boundary between "unstable" (below) and "sustained oscillations" (above) solutions discussed by *Segall and Rice* [1995]. R1–R3 mark locations of $\bar{k}$ of the seismogenic parts of the standard models discussed in section 7.1. Compare to Figure 6.

in the uppermost 3 km and below $z = -14$ km. Between these two zones a velocity-weakening region ($a < b$) allows instabilities to develop.

[19] Although the model can potentially be used to study explicitly fluid flow phenomena related to faulting, we focus here on fundamental response pattern resulting from either drained or undrained conditions. Therefore a necessary simplification is the imposed equality of pore pressure inside and outside the fault plane in excess of hydrostatic. The desired equality stems from the dependence of h_u^* on σ_e and thus on p (equation (15)). A physically more realistic hydrostatic pore pressure gradient in the crustal bulk in combination with an overpressured fault core and relatively high-permeable fault walls would cause the pore pressure in the fault to equilibrate over an amount of time determined by the actual diffusivity. Thus a temporal decrease of p in an initially overpressured fault zone bounded by permeable fault walls leads to a continuously decreasing h_u^* which we aim to avoid. Certainly, h_u^* depends on changes in ϕ, but these changes are shown to be minor and do not control the model's response because of a temporally variable critical cell size. By setting $p = p^\infty$ we leave p primarily a function of the second term in equation (8). As intended, pore compacting and dilatant processes determine pore pressure evolution rather than a (naturally probable) gradient between p and p^∞. Thus

$$p(x,z,0) = p^\infty(z) = \max\left[p_{\text{hyd}}(z), \sigma_n(z) - \tilde{p}\right], \qquad (16)$$

where $\tilde{p}$ is the difference between the lithostatic gradient and p (Figure 2b). Used values of $\tilde{p}$ result in different $\lambda = p/\sigma_n$ profiles (Figure 2c), controlling the response of an overpressured fault plane to external load.

[20] For computational reasons discussed in section 3.5 we use $f_\eta = 10^4$ throughout this study, emphasizing the investigation of the long-term slip evolution, and focusing to lesser extend on details associated with single instabilities. We repeat various simulations with $f_\eta = 1$ to document the validity of the obtained results for quasi-dynamic conditions. As outlined by equation (15), $\varepsilon\mu_0/\beta$ is a crucial parameter controlling the stability of a system in the undrained limit. Because our primary interest is the influence of dilatancy we keep $\mu_0 = 0.7$ and $\beta = 5 \times 10^{-4}$ MPa^{-1} constant.

[21] Values for diffusivity representing drained and undrained conditions are $c_d^* = 10^4$ yr^{-1} and $c_u^* = 10^{-4}$ yr^{-1}, respectively, which is supported by the graphical representation of equation (12) described in section 6. To compute shear stress $\tau(x, z, t)$, we evaluate equation (1) after each integration step, using $\tau^0 = 100$ MPa being scalar for simplicity. Actually, τ^0 represents the applied stress in the crust in the absence of driving forces, i.e., equation (4) with $\mu = \mu_0$, and a lithostatic and a hydrostatic gradient could have been used to obtain $\tau^0(z)$. The chosen value determines the absolute stress level on the fault, but since we are interested in relative stress changes $\tau^0 = 100$ MPa does not influence the conclusions.

6. Stability Regimes

[22] Figure 3 illustrates the dependence of the normalized critical stiffness $\bar{k}$ on hydraulic diffusivity for a specific value of λ. The normalization $\bar{k} = k^{cr}/k_d^{cr}$ is carried out using k_d^{cr}, because it is the maximum value for drained conditions at which $F(c^*)$ approaches zero (equation (12)). It allows an intuitive understanding of the system's response in terms of a simple spring block slider model, since $k > k^{cr}$ and $k < k^{cr}$ results in stable and unstable responses, respectively [*Ruina*, 1983]. The analysis of a 1-D model [*Segall and Rice*, 1995] reveals that different depth sections of the present 3-D

system can be situated in three possible stability regimes. For a drained fault ($c^* > 10^1$ yr^{-1}) the sign of $a - b$ controls the response mode, i.e., k^{cr} is defined only for $a < b$.

[23] For undrained properties the analysis of equation (12) indicates a bifurcation of $\bar{k} = \bar{k}(\varepsilon, c^*)$ in a transition zone between essentially drained and undrained regimes. In the undrained, frictionally unstable environment, two responses are possible. First, if ε is smaller than a critical value ε_{cr}, the 1-D system develops regular stick-slip behavior as under drained conditions. Second, dilatant processes are able to stabilize an otherwise unstable fault, leading to stable slip rates if $\varepsilon > \varepsilon_{cr}$. To determine ε_{cr}, equation (12) can be rewritten as

$$\varepsilon_{cr} = -\frac{\beta\sigma_n}{\mu_0}(\lambda - 1)(b - a). \quad (17)$$

Note that ε_{cr} is defined only for $a < b$ and depends on σ_n for various degrees of overpressurization, λ.

[24] *Segall and Rice* [1995] observed that for some range of $k < k^{cr}$ infinite oscillations persist, approximated by the dotted line in Figure 3. As shown in section 7.2, we do not observe this particular response of a 1-D model for a wide parameter range for drained conditions in our 3-D simulations, since observed k are smaller than k values associated with the oscillations response regime. However, we observe oscillations as a special case of nonuniform response pattern for undrained conditions (Section 7.5), because the depth dependence of ε_{cr} leads to a transition zone at constant c^* as a function of ε. Sections 7.4 and 7.5 will focus on the emergence of nonuniform spatiotemporal slip evolutions of models with parameters defining these transition zones.

7. Modeling Results

7.1. Reference Models

[25] We begin the discussion of modeling results with the validation of our procedure by comparing generated slip evolutions of a drained model to previously investigated results. A typical implementation example consists of a 100 km $\times$ 24 km fault zone discretized into 256 $\times$ 64 cells. Drained conditions are parameterized by $c^*_d = 10^4$ yr^{-1}, which is shown not to interact with a transition zone in Figure 3. The pore pressure profile follows equation (16) with $\bar{p} = 100$ MPa, which leads using $L = 0.03$ m to $h/h^* = 0.27$. The chosen value $\varepsilon = 10^{-4}$ has no influence on slip evolution, as revealed by the collapse of all $\bar{k} = \bar{k}(\varepsilon, c^*)$ lines for $c^* > 10$ yr^{-1} (Figure 3). The normalized critical stiffness $\bar{k}$ at seismogenic depth is located at R1 in Figure 3, and Figure 4a displays the typical stick-slip pattern of slip evolution of an arbitrarily chosen profile along the fault plane.

[26] We use $k = k^{sys} = \Delta\tau/\Delta u$ to determine the stiffness [*Dieterich*, 1992; *Kato and Hirasawa*, 1997] of a system, estimating the stress drop $\Delta\tau$ and coseismic slip Δu from computed results. We find that $\bar{k}$ of R1 is approximately 0.3, using $k^{cr}_d = 0.004 \times 100$ MPa/0.03 m to normalize k. Because $k > k^{cr}$ allows instabilities do develop, slip evolution in Figure 4a shows established features of slip evolution of previously performed rate- and state-controlled frictional strike-slip models [e.g., *Tse and Rice*, 1986; *Rice*, 1993; *Rice and Ben-Zion*, 1996; *Ben-Zion and Rice*, 1995; *Lapusta et al.*, 2000]. Stable sliding occurs in the velocity-strengthening regime below the seismogenic zone where $a > b$, with slip rates equal to v^∞ shown by the velocity evolution in Figure 4b of an computational point at 7 km depth somewhere along the fault's strike. In case $a < b$, accumulated strain energy is released in regular, unstable stick-slip behavior with an average repeat time of $\hat{t} = 101.8$ years. Corresponding velocities indicate the locking of the fault ($v \ll v^\infty$) at interseismic periods. Figures 4c–4e display corresponding temporal evolution of stress, porosity, and pore pressure, respectively. Slip events are associated with shear stress drops of 16 MPa, and $\varepsilon = 10^{-4}$ allows a coseismic porosity increase of about 1%. Interseismic periods exhibit gradual stress increase and porosity reduction. High diffusivity is responsible for an immediate equilibration of pore pressure states p and p^∞, leading to small pore pressure changes during slip events and a balanced pore pressure level between instabilities. Using $f_\eta = 1$ instead of $f_\eta = 10^4$ leads to higher coseismic slip rates, larger amplitudes of corresponding variables, and larger interevent times.

[27] We change conditions from drained to undrained by decreasing the effective diffusivity to $c^*_u = 10^{-4}$ yr^{-1}, which leads to $h/h^* = 0.25$; that is, variations in nucleation size compared to the previous case can be neglected. We also change ε from 10^{-4} to 2×10^{-5} to assure a regular stick-slip response of the system ($\bar{k}$ at seismogenic depth at R2 in Figure 3), but all other parameters are kept constant. Whereas the evolution of slip, velocity, and shear stress of an arbitrary cell at $z = -7$ km of this undrained model are comparable to the corresponding functions of the standard drained model (Figure 5a), the evolution of porosity and pore pressure changes differ. Slightly smaller stress drops of about 13 MPa lead to shorter interevent times of $\hat{t} = 87.3$ years. The dilatancy coefficient $\varepsilon = 2 \times 10^{-5}$ allows porosity increases of 0.1%, an order of magnitude smaller than those generated by $\varepsilon = 10^{-4}$ in the drained model. The significance of porosity changes on pore pressure evolution in the undrained limit is revealed by a coseismic drop in p, indicating that an increase in ϕ of 0.1% is sufficient to produce a pore pressure change of about 0.5 MPa. Positive $\dot{\phi}$ and small effective diffusivity result in elevated pore pressure in excess of the background level p^∞ during interseismic periods, suggesting the fault is weaker compared to the drained fault. This relative weakness is responsible for earlier onset of instabilities.

[28] The other end-member case of system responses is stable creep. Whereas previously applied $\varepsilon = 2 \times 10^{-5}$ leads to the discussed unstable stick-slip response, $\varepsilon > 2 \times 10^{-4}$ results in a creeping fault with slip rates $v = v^\infty$. Slip induced increase in pore space is sufficient to stabilize an otherwise unstable fault ($\bar{k}$ marked by R3 in Figure 3), because $\varepsilon > \varepsilon_{cr}$ for dominating depth sections. Slightly smaller values like $\varepsilon = 10^{-4}$ alter the type of response significantly shown later in section 7.5. Note that these particular responses, creep and nonuniform slip behavior as discussed below, cannot be produced by a purely elastic model with homogeneous frictional properties, since $a < b$ at seismogenic depth allows for instabilities at all times.

7.2. Effect of Diffusivity on Average Repeat Time

[29] The stability regime of reference model R1 is linked to regimes of both undrained models R2 and R3 for

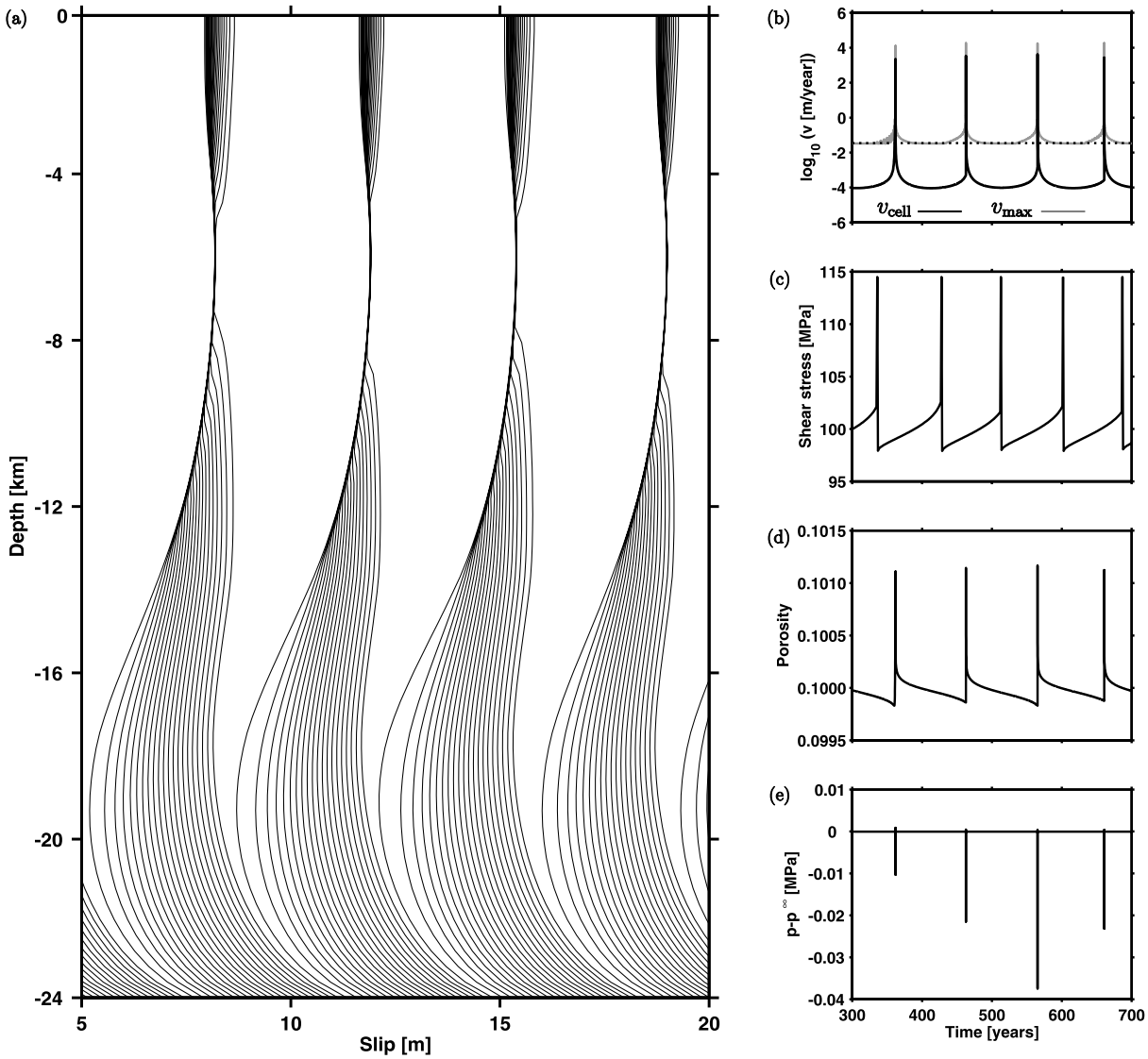

Figure 4. Results of the standard drained model R1 (see corresponding $\bar{k}$ in Figure 3). Parameters $c^* = 10^4$ yr^{-1}, $\varepsilon = 10^{-4}$, $\tilde{p} = 100$ MPa, $L = 0.03$ m, $X_{\text{length}} = 100$ km, $nx = 256$, $h/h^* = 0.27$, $f_\eta = 10^4$, $\mu_0 = 0.7$, $\beta = 5 \times 10^{-4}$ MPa^{-1}. (a) Cumulative slip evolution. Lines are drawn every 5 years. Sections at depth slide stable, whereas sections at seismogenic depth are locked in interevent times and slip seismically during an instability. (b) Velocity evolution. Dotted line represents v^∞. Solid black line shows the behavior of a cell at 7 km depth, v_{cell}, indicating locked interseismic periods because $v_{\text{cell}} \ll v^\infty$. Grey line displays the maximum slip rate on the fault plane at a given t, $v_{\max}$, indicating the lower part of the fault slips with $v = v^\infty$ during interseismic periods. (c)–(e) Corresponding evolution of shear stress, porosity and pore pressure change of a cell at $z = -7$ km. Different amplitudes of $p - p^\infty$ are due to hard disc space friendly sparse sampling of the continuous numerical solution (monitor every 10th of about 80,000 time steps) and high diffusivity, leading to instantaneous equilibration of the pore pressure states. Compare to Figure 5. For details see text.

decreasing c^* and different values of ε (Figure 3). An indicator of the existence of a transition of response types from drained to undrained regimes is the change of average repeat time of system-wide events, $\hat{t}$. Juxtaposed to the theoretical dependence of $\bar{k}$ on c^* in Figure 6a, Figure 6b shows $\hat{t}$ as a function of c^* for four systems with $\varepsilon = [10^{-5}, 5 \times 10^{-5}, 10^{-4}, 5 \times 10^{-4}]$.

[30] With $k = k^{\text{sys}}$ defined above, we find that $\bar{k}$ of systems discussed in Figure 6b is maximum 0.2–0.3. As expected, $k > k^{\text{cr}}$ since instabilities can develop. Observed low values of $\bar{k}$ correspond to the "unstable" regime in Figure 4 of *Segall and Rice* [1995]. It shows that k of current simulations do not fall into "sustained oscillations" parts of the parameter space, where $\bar{k}$ is considerably larger. In principle, the change of the crust's properties would allow a modification of K and hence k, but this tuning is beyond the scope of the present work.

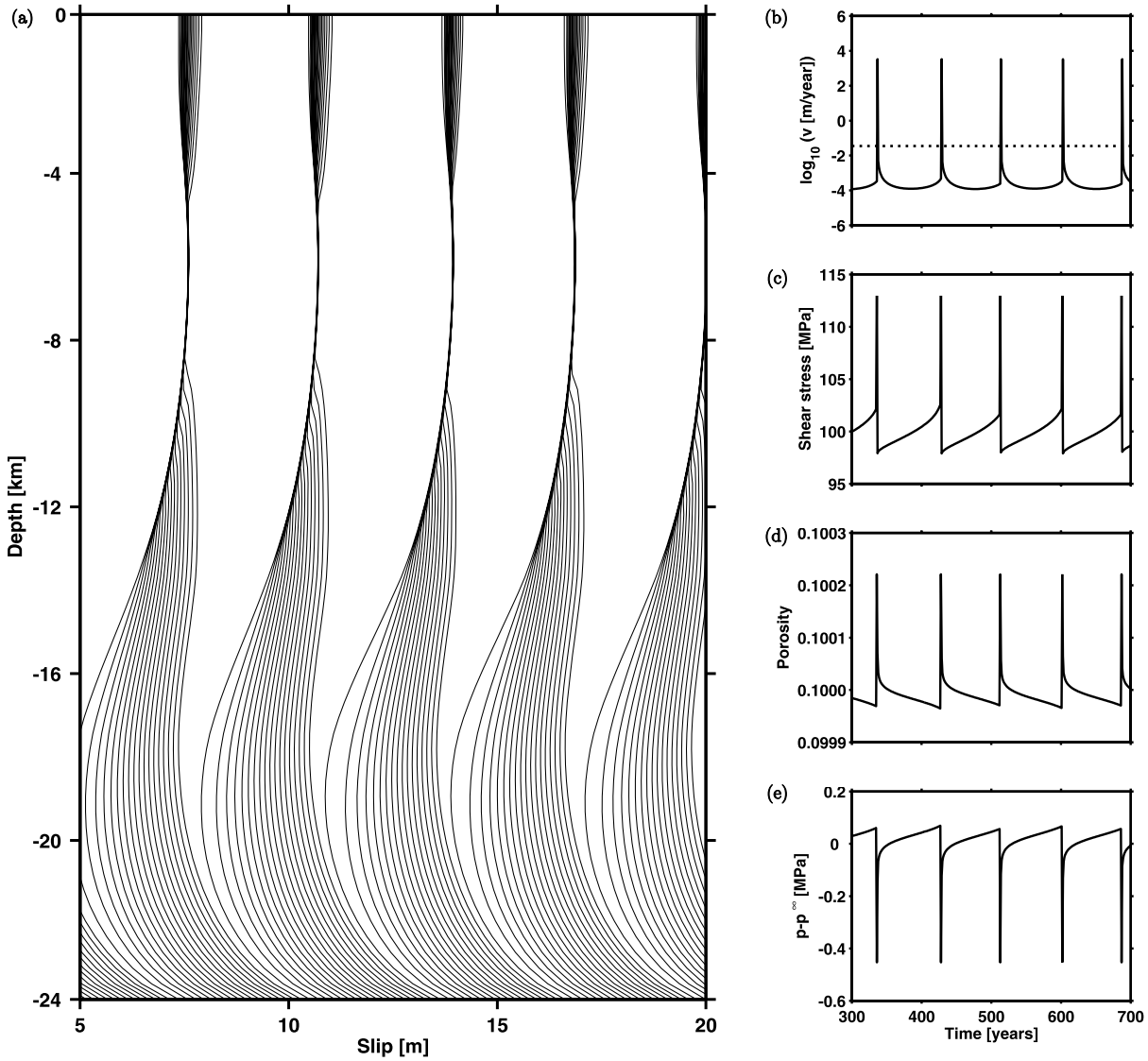

Figure 5. Results of the standard drained model R2 (see corresponding $\bar{k}$ in Figure 3). Parameters are as in Figure 4, except $c^* = 10^{-4}$ yr^{-1}, $\varepsilon = 2 \times 10^{-5}$, $h/h_u^* = 0.25$. (a) Cumulative slip evolution. Lines are drawn every 5 years. (b)–(e) Corresponding evolution of v_{cell} at $z = -7$ km, shear stress, porosity, and pore pressure change. For details see text. Note the similarity in slip, velocity and stress evolution to Figures 4a–4c, but different response characteristics between corresponding Figures 4d–4e. In particular, the coseismic pore pressure change is an order of magnitude larger compared to the drained model and $p > p^{\infty}$ during interseismic periods.

[31] The systematic decrease of $\hat{t}$ for $\varepsilon > 10^{-5}$, and the relatively constant $\hat{t}$ dependence for $\varepsilon = 10^{-5}$ toward more undrained conditions reflects the corresponding $\bar{k} = \bar{k}(\varepsilon, c^*)$ functionality. The decrease of $\hat{t}$ is in agreement with the fact that more stiff systems cannot sustain as large stresses as relatively compliant systems [*Segall*, 1996]. Hence they fail more easily and therefore more often, which is supported by the observed tendency of decreasing k^{sys} for decreasing c^* at constant ε. The physical interpretation for a significant reduction of $\hat{t}$ for $\varepsilon \geq 5 \times 10^{-5}$ toward decreasing c^* can be obtained from the evaluation of equation (12). For small c^* the right-hand side becomes sensitive to $\varepsilon\mu_0/\beta$ with respect to $\sigma_e(b - a)$. With the applied constant values for β and μ_0, the stabilizing effect of dilatant pore space increase at the onset of instabilities dominates for values of $\varepsilon \geq 5 \times 10^{-5}$. Hence relatively undrained conditions coupled to an effective dilatant mechanism cause coseismic slip to cease earlier compared to less effective pore space increase and the ability to equilibrate pressure states, respectively.

[32] It can be seen from Figure 6b that $\hat{t}$ for $\varepsilon \geq 5 \times 10^{-5}$ starts to decrease at larger diffusivities ($c^* \approx 10^3$ yr^{-1} for $\varepsilon = 5 \times 10^{-4}$, $c^* \approx 10^1$ yr^{-1} for $\varepsilon = [5 \times 10^{-5}, 10^{-4}]$) than the corresponding lines in Figure 6a suggest. The reason for this deviation from the theoretically derived 1-D approach can be seen in the explicit 2-D extension of the fault plane. Other parameters controlling the repeat time not investigated here are the damping factor f_η, the spatial extension of the model space, X_{length}, and the chosen discretization, h/h^*.

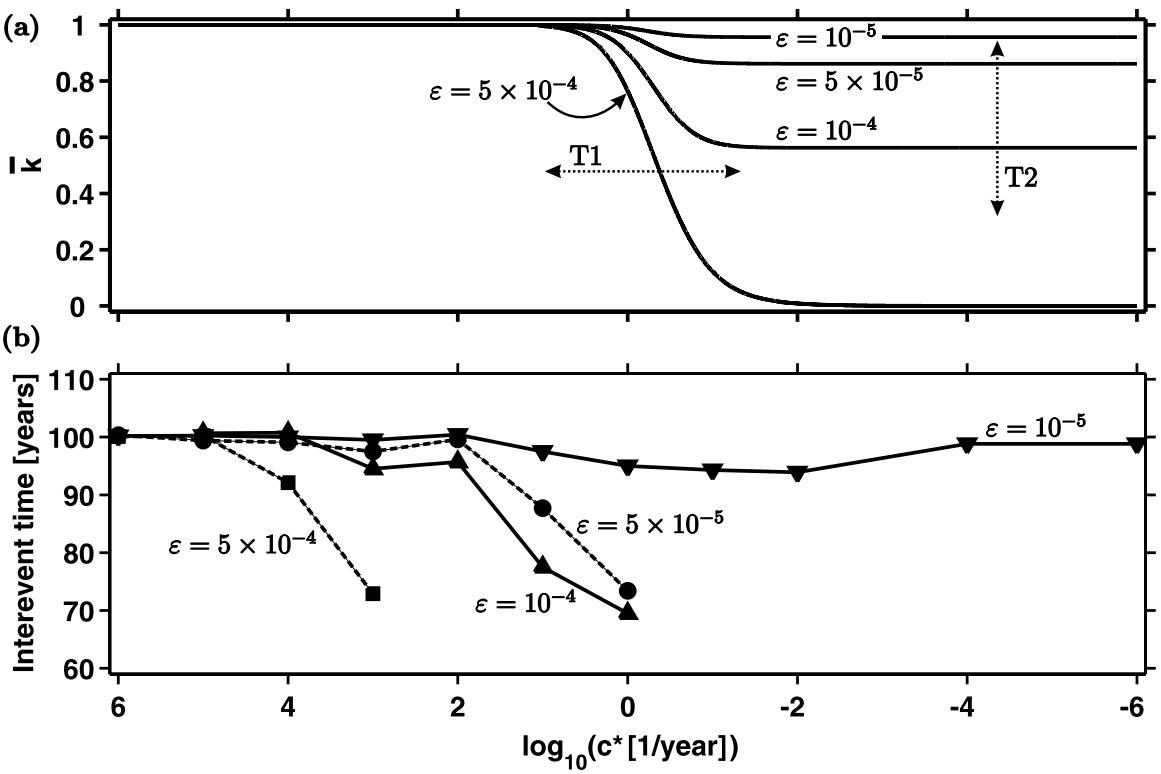

Figure 6. (a) Reproduction of Figure 3. T1, T2 indicate transition zones. T2 approximates the location of the horizon of the parameter space shown in Figure 8. (b) Average repeat times as a function of diffusivity, showing the same trend as $\bar{k}$ in Figure 6a, revealing the correspondence of critical stiffness and observed interevent times. For details see text.

Beyond $c^* = 10^0$ yr^{-1}, $\hat{t}$ of system-wide events cannot be measured any longer for simulations with $\varepsilon \geq 5 \times 10^{-5}$, since systems do not respond in a regular stick-slip manner but in a nonuniform way discussed in sections 7.4 and 7.5.

7.3. Terminology

[33] On the basis of the results shown in section 7.1 we clarify the terminology used in the discussion below. Strain release during episodic quasi-dynamic slip occurs with seismic slip velocities (Figures 4 and 5), leading to a periodic sequence of uniform system-wide or characteristic stick-slip events. As demonstrated (Figure 4), $f_\eta \gg 1$ results in slip rates during instabilities that are smaller than those observed in natural earthquakes ($\sim$1 m s^{-1}). *Hillers et al.* [2006] defined a threshold velocity to separate seismic from aseismic slip generated by 3-D rate- and state-controlled quasi-dynamic simulations using heterogeneous frictional properties, without producing realistic dynamic slip rates. Following their concept, we interpret periods of accelerated slip as intermittent quasi-dynamic instabilities, and $v \gg v^\infty$ are considered as seismic slip rates, even if simulated velocities do not reach values comparable to observed rates. Stable sliding or creep refers to slow slip rates on the order of v^∞, as found for deeper parts of the fault in Figures 4a and 5a. These creeping portions of the fault are assumed to behave aseismic. The seismogenic depth sections of the unstable stick-slip reference models are referred to as locked, since here v is up to three orders of magnitude smaller than the load velocity (Figure 4b). We use the terms nonuniform, complex or pattern-like to describe heterogeneous slip evolution along the fault's strike. We do not distinguish explicitly between aseismically accelerated or fast creep, respectively, and slow creep.

7.4. Transition I: From Drained to Undrained Conditions

[34] So far we investigated the behavior of systems whose location in the parameter space resulted in characteristic slip events or stable creep. We now focus on the behavior of systems situated in a transition between the clearly defined stable and unstable regimes. First, we continue to decrease the diffusivity beyond conditions that are drained for time periods during slip events. As indicated by Figure 6, for systems with $\varepsilon = 10^{-4}$ $\hat{t}$ can be obtained only for $c^* \geq 1$ yr^{-1}. More undrained systems with $c^* < 1$ yr^{-1} and $\varepsilon = 10^{-4}$ respond in a more complex way, explored by a representative model in T1 with $c^* = 10^{-2}$ yr^{-1} (Figure 6a). The resulting nonuniform slip pattern is displayed in Figure 7a, demonstrating that an instability does not develop into a system-wide event (e.g., at $x = 50$ km, $u \approx 12.5$ m). The slip deficit around this instability is reduced during a period of bilateral creep with variable slip rates. After two system-wide events ($u = 14.5$–17 m) an alternating pattern of stable sliding and small instabilities is established, with coseismic slip initiating where stress concentrations of creeping sections interact.

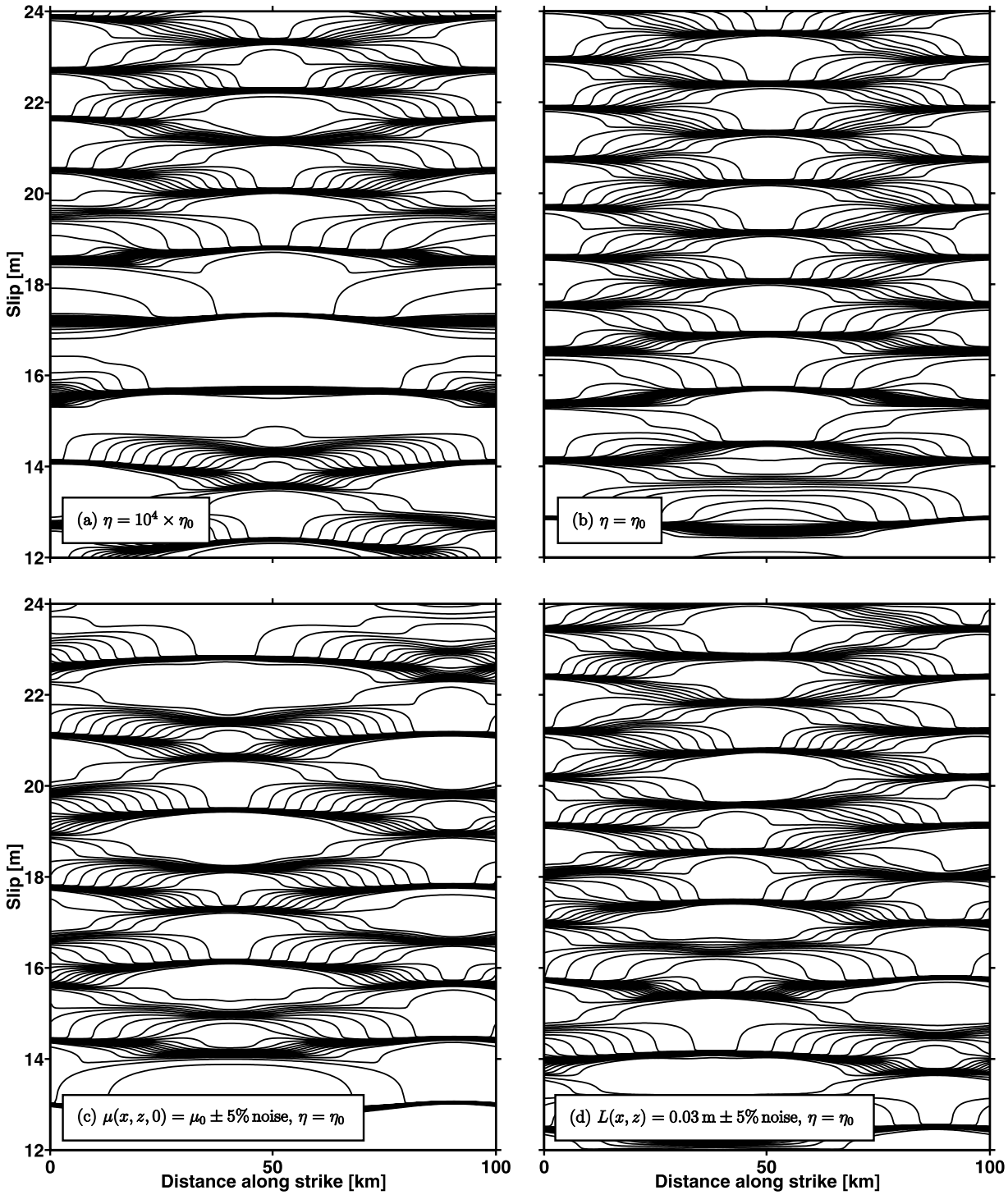

Figure 7. Pattern-like spatiotemporal slip evolutions of models in transition zone T1 (Figure 6a). Invariant parameters are $c^* = 10^{-2}\,\mathrm{yr}^{-1}$, $\varepsilon = 10^{-4}$, $\tilde{p} = 100$ MPa, $L = 0.03$ m, $\mu_0 = 0.7$, $\beta = 5 \times 10^{-4}\,\mathrm{MPa}^{-1}$, $X_{\mathrm{length}} = 100$ km, $nx = 256$, and $h/h^* = 0.24$. Lines are drawn every 2 years. (a) Plot of $f_\eta = 10^4$. See Figure 12c for $v_{\max}$, black line. (b) Plot of $f_\eta = 1$. See Figure 12 for $v_{\max}$, grey line. (c) Additional (fading) noise added to initial values of the friction coefficient, $f_\eta = 1$. (d) Quenched heterogeneity. Additional (persistent) noise is added to the critical slip distance L, $f_\eta = 1$.

[35] The modeling suggests that dilatancy hardening processes decelerate the slip rates of a developing instability to aseismic velocities (e.g., at $x = 50$ km, $u = 20$ m). Once sufficient pore space is created, simultaneous reduction of p and corresponding increase of the effective normal stress lead to the onset of dilatancy hardening that stabilizes slip. Subsequent creeping periods develop after a time period controlled by c^* sufficient to equilibrate p and p^∞ (compare to Figure 5e). Figure 7a shows the change of the resulting pattern during several cycles, with alternating sequences of

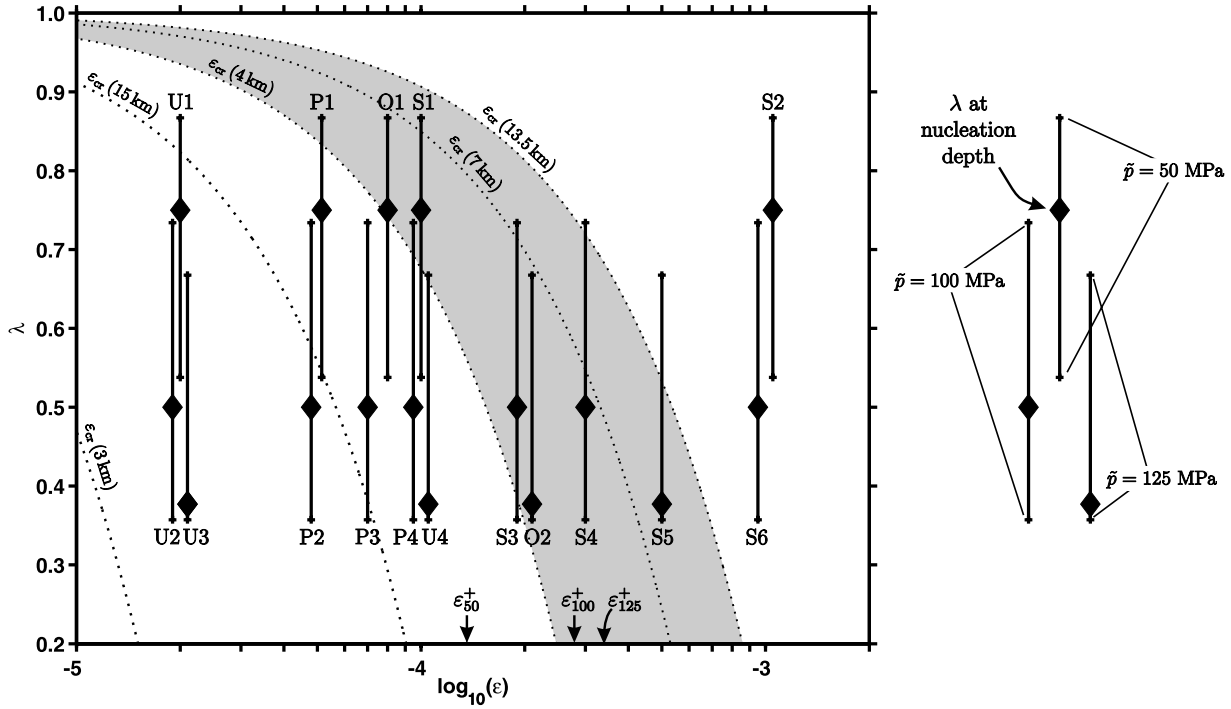

Figure 8. Parameter space $\lambda = \lambda(\varepsilon)$. U, P, O, and S denote observed response types unstable, pattern-like, oscillating and stable, respectively. Grey shaded zone illustrates ε_{cr} at seismogenic depth where $b - a = 0.004 = \text{const}$. Vertical lines represent λ values in the $b - a = 0.004$ depth section. The lines' vertical position and extension depends on $\tilde{p}$. Solid diamonds mark λ at nucleation depth. Left of $\varepsilon_{\tilde{p}}^{+}$ marked by arrows at the abscissa h^*_u is defined for each $\tilde{p}$ model set, whereas to the right $h^*_u < 0$ and therefore the response is stable. See Table 1 for a summary of results.

unstable and stable slip, in addition to system-wide events. Thus homogeneous hydromechanical and frictional properties are sufficient to generate nonuniform spatiotemporal slip evolution as a result of pore pressure controlling physical mechanisms.

[36] It is important to verify that basic characteristics of Figure 7a are a generic result of dilatancy hardening mechanisms, and that they are persistent choosing different geometrical and/or frictional parameters. Figure 7b shows the slip evolution for the same set of parameters except $f_\eta = 1$. Clearly, some second-order features do not persist, but the overall response pattern consists of alternating unstable and stable fault sections. To explore the origin of symmetry around $X_{\text{length}}/2$ in Figures 7a and 7b, we performed simulations with noise added to a variable or parameter, respectively. Figure 7c shows the result of a simulation with random noise being added to initial conditions of the friction coefficient, $\mu(x, z, 0) = \mu_0 \pm 5\%$ noise, whereas Figure 7d is produced using quenched heterogeneity by choosing $L(x, z) = 0.03$ m $\pm$ 5% noise. Heterogeneity in the initial conditions leads to a persistent shift of the symmetry axis, whereas the use of quenched heterogeneity results in the loss of a time invariant axis of symmetry. This suggests the symmetry observed in cases with homogeneous hydromechanical properties along strike is a finite size effect of the model fault due to the application of relatively few cells covering a relatively short fault zone (compare to dimensions of *Rice* [1993], *Liu and Rice* [2005], and *Hillers et al.* [2006]). In this case, repetitions of 10 faults along strike in each direction may not be sufficient to approximate infinite periodic boundary conditions. A symmetric pattern is even generated by computationally expensive simulations with $X_{\text{length}} = 200$ km and constant numerical discretization, and by a case with doubled nx and nz while bisecting L on a 100 km long fault, respectively. This indicates that at present computational limits do not allow to study a possible break in symmetry in the absence of finite size effects.

7.5. Transition II: Undrained Conditions

7.5.1. Response Types in the Parameter Space

[37] Section 7.4 dealt with reductions of c^* while keeping ε constant. Now we investigate the effect of ε on slip evolution for constant undrained conditions ($c^*_u = 10^{-4}$ yr^{-1}). Figure 8 shows the transition T2 displayed in Figure 6a for a particular depth section, i.e., for a particular set of a, b, λ, as an alternative horizon of the multidimensional parameter space. We used equation (17) to obtain the dependence of λ on ε. In the 1-D model of *Segall and Rice* [1995], a specific ε_{cr} can be determined to separate stable ($\varepsilon > \varepsilon_{cr}$) from unstable ($\varepsilon < \varepsilon_{cr}$) regimes. In the present 3-D fault model this boundary expands to a zone, because the frictionally unstable portion of the fault between 4 and 13.5 km depth ($a - b = 0.004 = \text{const}$) occupies an extended range in the diagram, represented by the grey shaded region in Figure 8. Values for depth regions for the smallest positive $b - a$ at about 3 and 15 km depth are plotted for reference, indicating an orientation of the transition zone

toward smaller ε values. This shows ε_{cr} is not constant throughout the plane but rather a function of depth. Hence different depth sections with different 1-D response types that depend on their location in the parameter space, when considered isolated, interact through K, leading to complex slip evolutions.

[38] The vertical lines in Figure 8 represent λ values at depths where $b - a = 0.004$ = const for a specific simulation. They show that these locations cannot be specified uniquely. Capital letters S, O, P and U denote stable, oscillating, pattern-like and unstable response types, respectively. The length of individual lines corresponds to applied $\tilde{p}$ values, such that the set of lines ranging from $0.54 < \lambda < 0.87$, $0.35 < \lambda < 0.73$ and $0.35 < \lambda < 0.67$ represent systems with $\tilde{p}$ = [50, 100, 125] MPa, respectively. The solid diamonds at each line indicate λ at 7 km depth where instabilities tend to nucleate. Different values of $\tilde{p}$ change h^* and thus h/h^* on an invariant computational grid with constant L. This could give rise to systematic artefacts in certain model responses. To rule out this possibility, we repeated selected simulations using different values for L and thus h^*, while keeping $\tilde{p}$ constant. No significant change in the response pattern has been detected, so that we are comfortable that our first-order results do not depend on the underlying discretization of the model space. While any given L does not influence the sign of h_u^*, L does control the actual nucleation size. It is therefore possible to systematically choose a certain L for each particular system to keep h/h^* constant for all simulations. We refrain from using this option since we want to change only λ and ε for a set of simulations to study the very effect of the two hydraulic parameters.

[39] As equation (15) reveals, h_u^* is defined only (i.e., $h_u^* > 0$) if ε is less than $\beta[\sigma_e(b-a)]_{max}/\mu_0$. Defining $\varepsilon_{\tilde{p}}^+$ as the maximum ε value that makes h_u^* positive for a specific degree of overpressurization, $\varepsilon_{\tilde{p}}^+$ has to be larger than 1.4×10^{-4}, 2.9×10^{-4}, and 3.6×10^{-4} for systems with $\tilde{p}$ = [50, 100, 125] MPa, respectively. These values are indicated by small arrows at the abscissa in Figure 8. Systems located to the right of their corresponding arrow (S2, $\varepsilon = 10^{-3} > \varepsilon_{50}^+$; S4, $\varepsilon = 3 \times 10^{-4} > \varepsilon_{100}^+$; S5, $\varepsilon = 5 \times 10^{-4} > \varepsilon_{125}^+$; S6, $\varepsilon = 10^{-3} > \varepsilon_{100}^+$) undergo stable creep throughout their entire depth, because the criterion $h_u^* > 0$ is never met down the fault [*Taylor and Rice*, 1998]. Models S1 and S3, however, respond in a stable fashion having $\varepsilon < \varepsilon_{\tilde{p}}^+$. Here, h_u^* is defined and thus the cause for stable creep is not $h_u^* < 0$. Rather, these models correspond to the standard creeping model introduced in section 7.1, that is, their location in the $\lambda = \lambda(\varepsilon)$ plane indicates that dilatant processes suppress instabilities. In agreement with *Segall and Rice* [1995], the fault slips stably with $v = v^\infty$ after an initial phase of compaction.

[40] Differences in nucleation size do not lead to stable response. For example, the estimate of the nucleation zone of model S1 (h_u^* = 9.54 km, Table 1) is on the order of the seismogenic width of the fault, which makes the development of slip instabilities unlikely [*Hillers et al.*, 2006]. A repetition of the simulation changing L to 0.015 m and h_u^* = 4.77 km generates the same creeping response, as does model S3 with the same value for h^* but different $\tilde{p}$ and L. This demonstrates bisecting L does not change the response type, even in a sensitive region of the parameter space (O1 is located next to S1). Note that h_u^* for the unstable responding model U4 ($\tilde{p}$ = 125 MPa) is 4.24 km, a value close to h_u^* = 4.77 km of creeping S1 and S3. Thus a positive h_u^* and specific L are important, but in this case not controlling quantities. Instead, the particular parameterization, i.e., the degree of overpressurization coupled to a specific dilatancy coefficient, is responsible for the creeping response.

[41] We observe for each of the three model sets with a specific $\tilde{p}$ a transition from unstable to stable response as a function of increasing ε. However, this transition from stick slip to creep does not occur instantaneously, at a specific value of ε. Certain simulations reveal a pattern-like or sometimes oscillating response. As $\tilde{p}$ decreases, this transitional behavior tends to be located toward smaller ε with respect to the $\tilde{p}$ = 125 MPa set, but the main U $\rightarrow$ P/O $\rightarrow$ S sequence with increasing ε remains persistent. Possible reasons for this shift are as follows:

[42] 1. Critical values for $\varepsilon_{\tilde{p}}^+$ to assure $h_u^* > 0$ show the same order as the discussed shift toward smaller ε values of the pattern-like response zone, i.e., $\varepsilon_{125}^+ > \varepsilon_{100}^+ > \varepsilon_{50}^+$. Therefore a system with a lower degree of overpressurization is more unstable for a certain position on the ε axis. For smaller λ, h_u^* is smaller and thus instabilities are more likely to nucleate, compared to a more overpressured system.

[43] 2. As indicated by the dashed lines, ε_{cr} values for $0 < (b - a) < 0.004$ appear to be smaller than those in the grey shaded zone, indicating that different depth horizons become unstable at dilatancy regimes different from those of the seismogenic depth section.

[44] 3. One of the conditions for the onset of instability is the degree of overpressurization at the depth level of the nucleation itself. As the solid diamonds at each vertical bar indicate, the nonlinear depth dependence of λ (compare Figure 2c) places systems with $\tilde{p}$ = 125 MPa at relatively greater distance from ε_{cr} at nucleation depth. The other extreme pose systems with $\tilde{p}$ = 50 MPa since here λ at 7 km depth is closer to the section where the corresponding 1-D response is stable. Evidence for the significance of the degree of overpressurization are the responses of three models for which $\varepsilon = 10^{-4}$: System U4 ($\tilde{p}$ = 125 MPa) behaves in the regular stick-slip behavior, and slip evolution of P4 ($\tilde{p}$ = 100 MPa) is nonuniform, whereas S1 ($\tilde{p}$ = 50 MPa) creeps stably.

7.5.2. Nonuniform Response Pattern

[45] We conclude this section by discussing some nonuniform response pattern obtained in the systematic study of relevant parameters. In Figure 9 we plot slip evolutions of models P4, P1, and P3, where the upper and lower row shows responses generated with $f_\eta = 10^4$ and $f_\eta = 1$, respectively. For P3 and P4, $\tilde{p}$ = 100 MPa, and P1 has $\tilde{p}$ = 50 MPa. Dilatancy coefficients do not differ significantly among the three realizations, ranging from 5×10^{-5} to 10^{-4} for P1 and P4, respectively. Using $f_\eta = 10^4$, the slip evolution of P1 (Figure 9a) shows qualitatively the same features as the nonuniform slip pattern discussed in Figure 7. We observe some system-wide events with less coseismic slip compared to responses shown in Figure 9b due to low effective normal stresses, interrupted by periods of creep and smaller slip instabilities. At $u > 20$ m a pattern of alternating instabilities and creep evolves, similar to the one

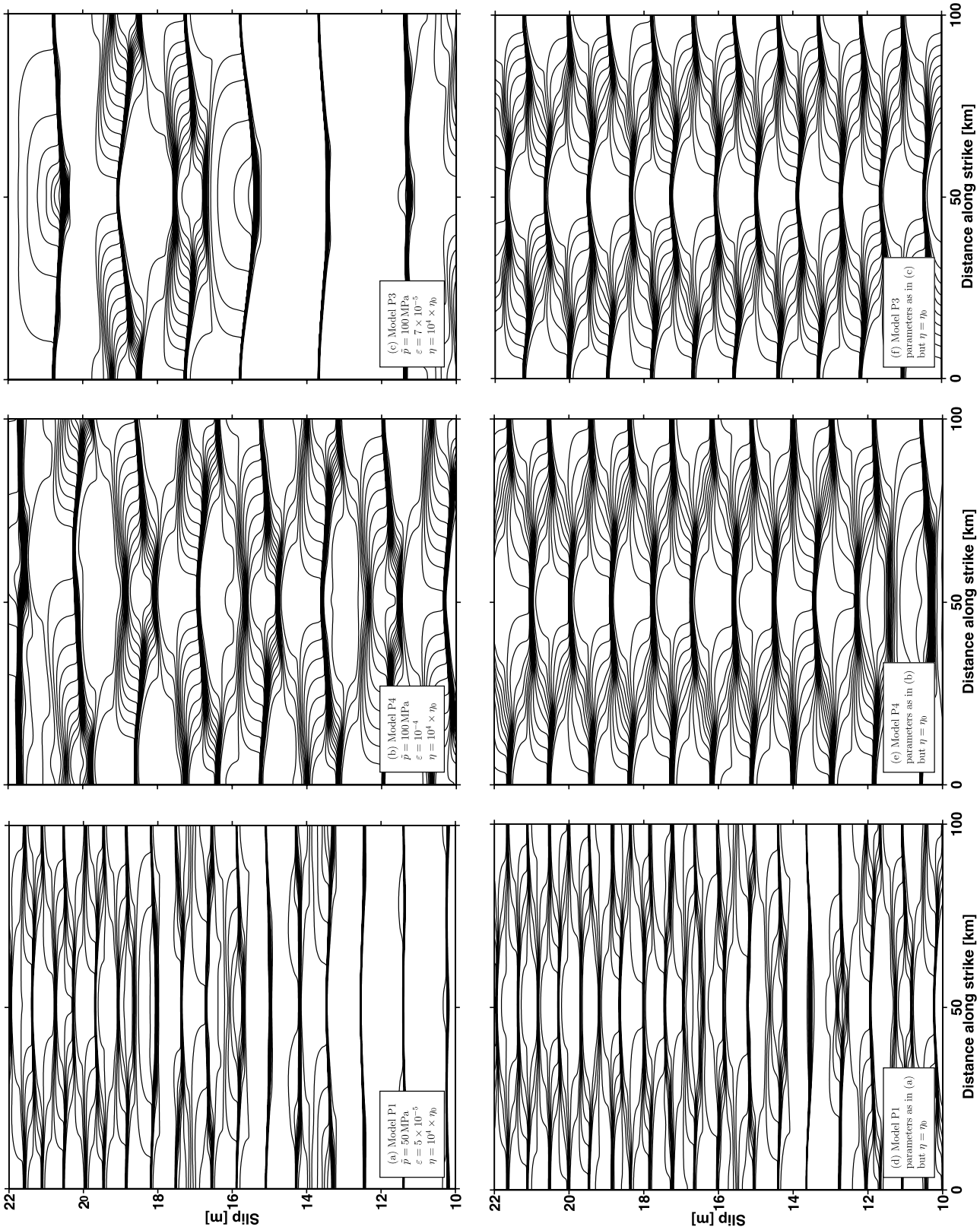
(a) Model P1
$\bar{p} = 50$ MPa
$\varepsilon = 5 \times 10^{-5}$
$\eta = 10^4 \times \eta_0$
(b) Model P4
$\bar{p} = 100$ MPa
$\varepsilon = 10^{-4}$
$\eta = 10^4 \times \eta_0$
(c) Model P3
$\bar{p} = 100$ MPa
$\varepsilon = 7 \times 10^{-5}$
$\eta = 10^4 \times \eta_0$
(d) Model P1
parameters as in (a)
but $\eta = \eta_0$
(e) Model P4
parameters as in (b)
but $\eta = \eta_0$
(f) Model P3
parameters as in (c)
but $\eta = \eta_0$
Slip [m]
Distance along strike [km]
10
12
14
16
18
20
22
0
50
100

Figure 9

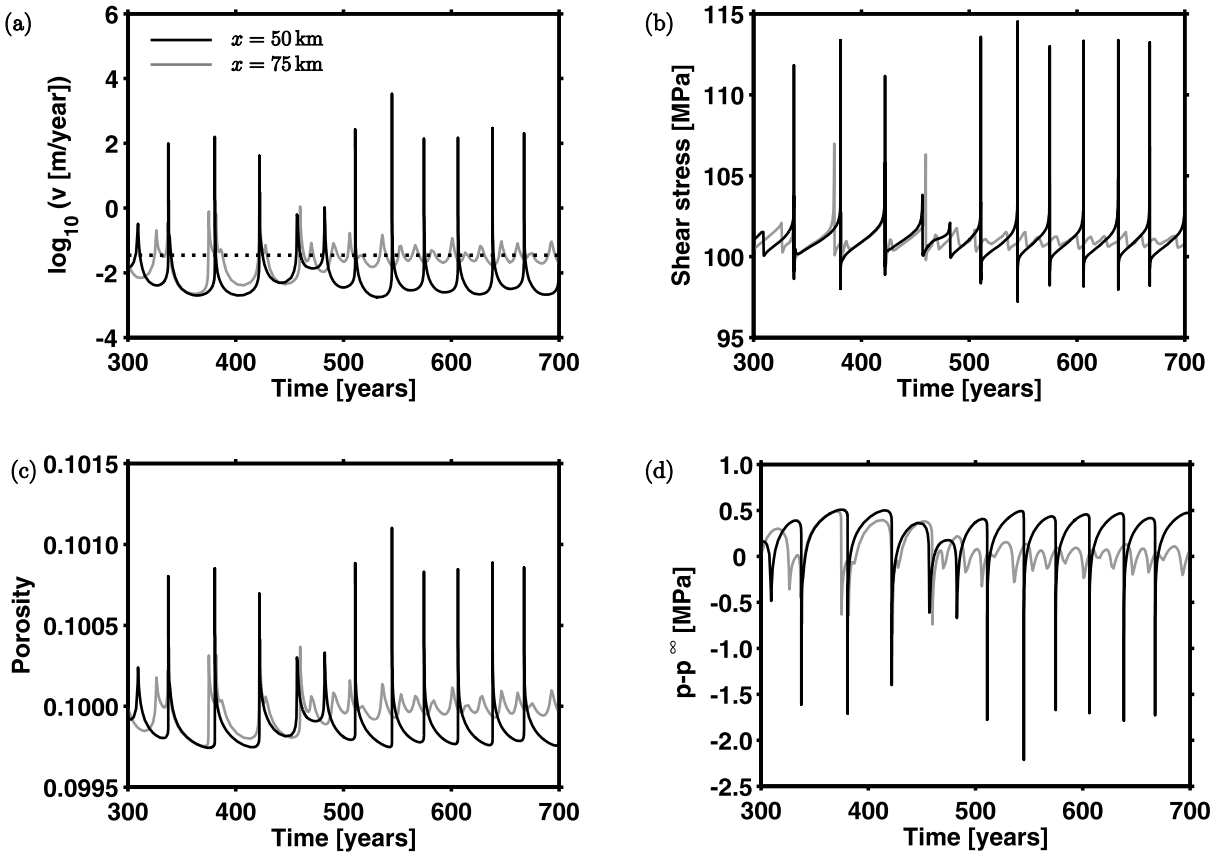

Figure 10. Response of two cells at $z = -7$ km and $x = 50$ km and $x = 75$ km, respectively, for a pattern-like response type of model P4 with $f_\eta = 1$ (Figure 9e). Evolution of (a) slip velocity, (dotted line illustrates v^∞), (b) shear stress, (c) porosity, and (d) pore pressure change. Note the difference in behavior for $t > 500$ years.

discussed in Figure 7. Compared to P1, model P4 ($\varepsilon = 10^{-4}$, Figure 9b) develops extended regions of creep, and intermittent slip events vary in size. Interestingly, the pattern's symmetry is broken at $u > 20$ m which is possible to happen at other simulations after sufficiently long simulation time. A different pattern evolves when ε is changed to $\varepsilon = 7 \times 10^{-5}$ (Figure 9c), indicating the change of response pattern is caused by the 30% difference of ε between P4 and P3. Particularly, in model P3 two system-wide stick-slip events occur between $u = 13.5$ m and $u = 17.5$ m, which do not evolve in model P4. Moreover, events of P3 for $u > 18$ m show larger coseismic slip than corresponding events in P4, a direct consequence of the smaller ε, since higher slip rates are required to produce the same change in porosity compared to more effective dilatant hardening.

[46] To discuss a homogeneous data set, all numerical experiments necessary to compile Figure 8 were performed using $f_\eta = 10^4$. We repeat all simulations except those where $h^* < 0$ using $f_\eta = 1$ to verify the robustness of observed slip evolutions without removing energy from the system through overdamped radiation. Figure 9d confirms the overall trend observed in Figure 9a, except showing a reduced tendency to generate system-wide events. Pattern shown in Figures 9e and 9f lack some characteristics of corresponding pattern in Figures 9b and 9c, respectively. The generated slip evolutions show regular sequences of creep and coseismic slip that persist in space and time. Results are thus sensitive to the degree of damping, but general characteristics and hence conclusions remain unaffected.

[47] We plot velocity, stress, porosity, and pore pressure change evolution of two computational points at $z = -7$ km, $x = 50$ km and $x = 75$ km, respectively, of model P4 with $f_\eta = 1$ (Figure 10). The response functions illustrate that some areas of the fault tend to behave in a more unstable way by having significantly accelerated slip rates ($v \gg v^\infty$) during instabilities and sufficiently reduced velocities ($v \ll v^\infty$) in interseismic periods, whereas nearby areas exhibit creeping slip rates on the order of v^∞. The evolution of τ, ϕ and $p - p^\infty$ is coupled to the velocity evolution as described in the undrained reference model (Figures 5d and 5e). Note that $\varepsilon = 10^{-4}$ allows for pore pressure changes of up to

Figure 9. Nonuniform spatiotemporal slip evolution from selected models P1, P4, and P3 (Figure 8) in the undrained limit, located in transition zone T2 (Figure 6a). For parameters, see insets and Table 1. Lines are drawn every 2 years. (a)–(c) Plots of $f_\eta = 10^4$ (See Figures 12d–12f, black lines, for v_{max}.) (d)–(f) Responses to identical parameter set as in the upper row except $f_\eta = 1$ (see Figures 12d–12f, grey lines, for v_{max}).

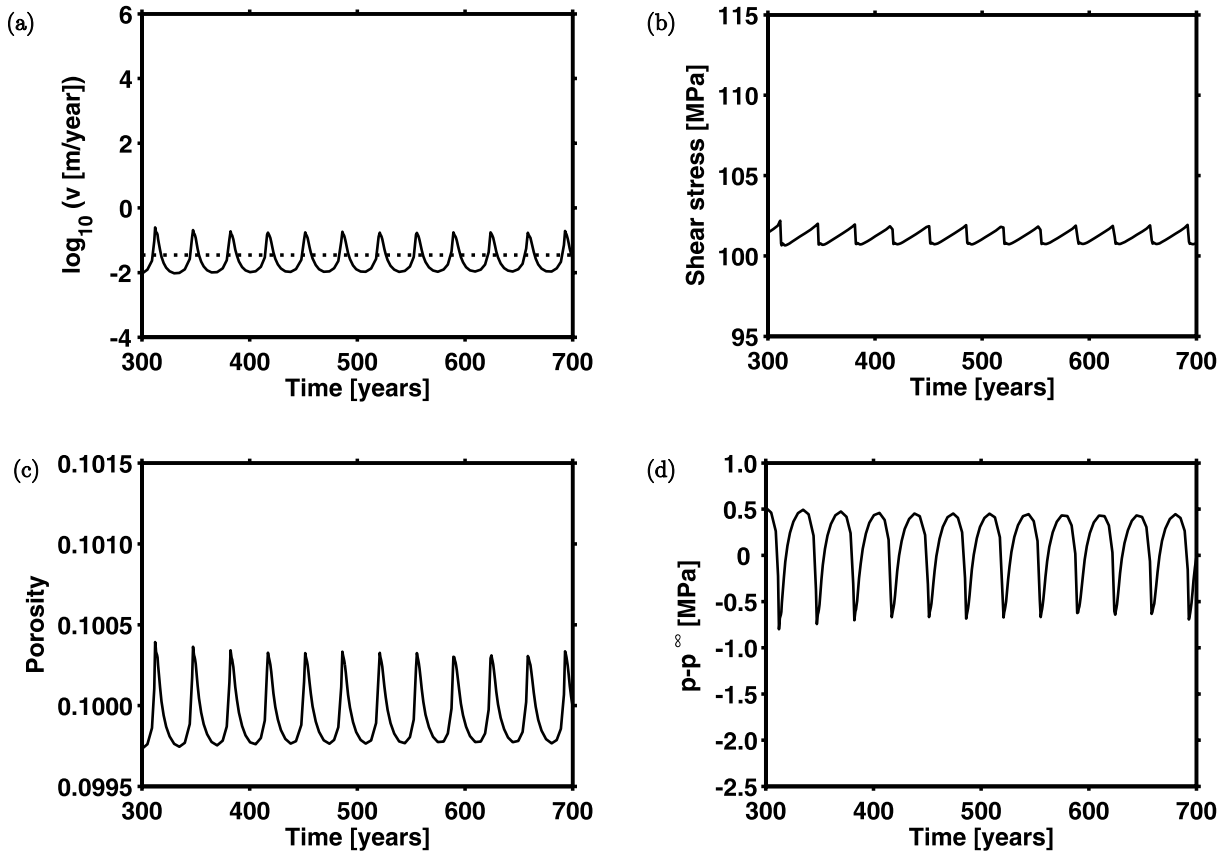

Figure 11. Response of an arbitrarily chosen cell at seismogenic depth of an oscillating response type of model O2 with $f_\eta = 1$. Evolution of (a) slip velocity (dotted line illustrates v^∞), (b) shear stress, (c) porosity, and (d) pore pressure change.

2 MPa, compared to changes of 0.4 MPa shown in Figure 5 with $\varepsilon = 2 \times 10^{-5}$.

[48] A particular response type are sustained oscillations as of model O2 (Figure 11) which generates slip rates fluctuating around v^∞ (Figure 11a), and corresponding small stress fluctuations (Figure 11b). A relatively large dilatancy coefficient of $\varepsilon = 2 \times 10^{-4}$ is responsible for porosity changes of 0.5%, associated with changes in pore pressure of about 1 MPa, and $p > p^\infty$ when slip rates are smallest. Note that these oscillations are a product of models situated in a region of the parameter space that does not correspond to those observed by *Segall and Rice* [1995]. While they observed oscillating behavior for a wider range of $0.9 < \bar{k} < 0.4$ and $c^* > 1$ yr^{-1}, we observe this response only for two specific parameter choices in the undrained limit. This discrepancy can be attributed to the spatial extension of the model space and associated interactions in the present study.

[49] Figure 12 summarizes velocity evolutions that correspond to simulations used to discuss generic response types observed in this study. Figures 12a and 12b illustrate the effect of different damping on regular stick-slip behavior, i.e., overdamping removes energy from the system more effectively leading to shorter interevent times. The slip rate during instabilities of both parameter sets is interpreted as being seismic. Velocities of models generating nonuniform slip evolution (Figures 12c–12f) are shown to produce different patterns depending on f_η, but significantly accelerated slip justifies the label "seismic" for intermittent instabilities using $f_\eta = 1$ or $f_\eta = 10^4$, even though slip rates do not reach values as in Figures 12a and 12b. Velocities of about $v \approx 10$ m yr^{-1}, like the "plateaus" visible in Figure 12f at $t = [350, 400, 450]$ years, can be interpreted as fast but aseismic creep. Generally, not overdamped simulations produce larger slip rates. Figures 12g and 12h illustrate $v_{\max}(t)$ of sustained oscillations and stable creep, respectively.

8. Discussion

[50] In our analysis of the parameter space of a 3-D fluid-infiltrated rate- and state-controlled fault model we observe three different types of spatiotemporal slip evolution. First, in agreement with previously discussed work using homogeneous frictional properties [*Tse and Rice*, 1986; *Rice*, 1993; *Ben-Zion and Rice*, 1995; *Rice and Ben-Zion*, 1996; *Lapusta et al.*, 2000], models in the drained limit develop the typical seismic stick-slip behavior of repeating characteristic earthquakes. Interevent times are found to depend on hydraulic diffusivity and dilatancy coefficient, in agreement with theoretically derived values of the critical stiffness. Second, in the undrained limit, a relatively large dilatancy coefficient leads to stable aseismic creep of the entire fault. Third, the extension of the undrained 1-D model to two

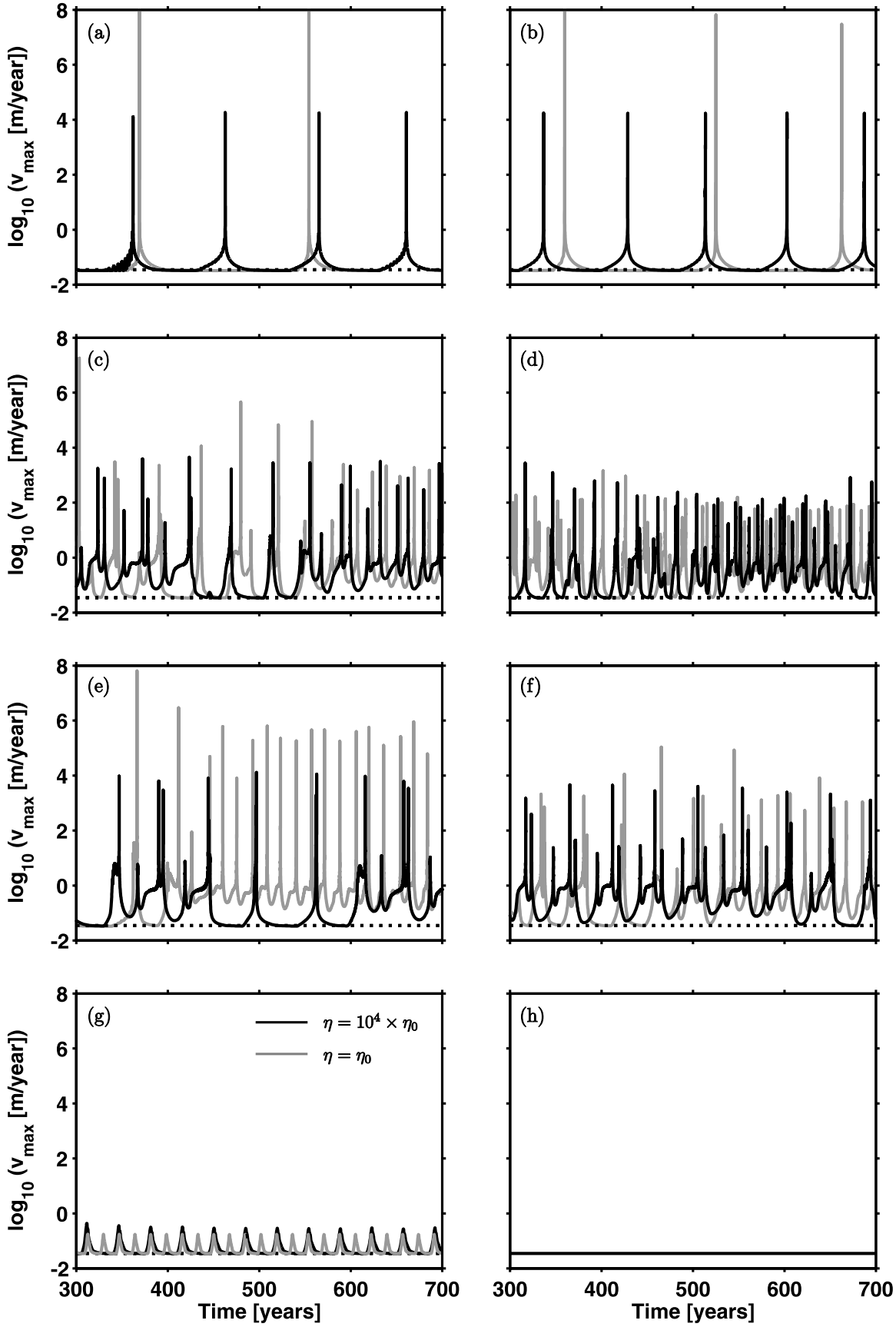
(a)
(b)
(c)
(d)
(e)
(f)
(g)
(h)
$\log_{10}(v_{max}$ [m/year])
$\eta = 10^4 \times \eta_0$
$\eta = \eta_0$
Time [years]
300
400
500
600
700
8
6
4
2
0
-2

Figure 12

dimensions explored here leads to nonuniform spatiotemporal slip pattern with alternating seismic slip, and aseismic creep of variable slip rates. Those patterns are not artifacts of the numerical procedure since their occurrence is persistent for all degrees of overpressurization, degrees of damping, and variable L values used in some test cases. Some characteristics of irregular slip evolution demonstrated by simulations with parameters located in transitional stability regimes bounded by stable and unstable regimes are as follows.

[51] A persistent feature is the episodic occurrence of instabilities followed by stable, aseismic creep. In terms of natural seismicity, dilatant processes slow down an earthquake from coseismic slip velocities to creeping velocities. Slip at these velocity regimes is referred to as stable afterslip. In agreement with our modeling results, afterslip has been reported to occur in regions surrounding the coseismic slip regions of the 2003 Tokachi-oki earthquake [*Miyazaki et al.*, 2004]. *Bürgmann et al.* [2002] modeled afterslip of the 1999 Izmit earthquake. In this case, afterslip was observed between those parts of the fault that slipped coseismically. *Hearn and Reilinger* [2002] discussed possible processes that lead to this particular behavior, favoring $a > b$ controlled velocity-strengthening friction. However, the standard interpretation of laboratory data suggest that values of a and b at seismogenic depth are unlikely to produce stable creep. In contrast to *Hearn and Reilinger* [2002] we suggest dilatancy induced postseismic creep, since this allows simpler, uniform frictional properties on the fault surface. Subsequent slip events nucleate where tip regions of creeping sections interact as a result of periodic boundary conditions. Whereas boundary conditions can be considered being artificial, the onset of instabilities due to creeping stress concentrations provides a possible mechanism for earthquake nucleation. At least two of the models show behavior that switches between different types of slip evolution, where system-wide events are preceded and followed by creeping periods. The larger the degree of overpressurization in excess of hydrostatic, $\tilde{p}$, the less coseismic slip occurs. However, comparing simulations with the same $\tilde{p}$ but different ε shows that coseismic slip also depends on dilatancy.

[52] It has been shown that complex features of observed natural seismicity such as the occurrence of the Gutenberg-Richter (GR) statistics and aftershock pattern cannot be generated by rate- and state-controlled models in the continuum limit with homogeneous frictional properties [e.g., *Tse and Rice*, 1986; *Rice*, 1993; *Ben-Zion and Rice*, 1997; *Lapusta et al.*, 2000], but by inherently discrete model realizations [e.g., *Burridge and Knopoff*, 1967; *Langer et al.*, 1996; *Carlson and Langer*, 1989; *Bak et al.*, 1987; *Ito and Matsuzaki*, 1990; *Lomnitz-Adler*, 1993; *Ben-Zion*, 1996; *Zöller et al.*, 2005]. *Cochard and Madariaga* [1996], *Nielsen et al.* [2000], and *Shaw and Rice* [2000] confirmed that generation of slip complexity on a homogeneous fault requires special choices of constitutive and model parameters. Here we have shown that heterogeneous slip pattern can be generated with a continuous fault description using homogeneous frictional and hydromechanical properties along strike.

[53] As summarized by *Ben-Zion* [2001] intrinsic properties of the governing (drained) frictional law is not observed to be sufficient to generate complexity in the continuum class of models. Rather, heterogeneous slip evolution has been shown to be associated with the $a - b$ induced velocity-weakening to -strengthening transition at 15 km depth [*Lapusta et al.*, 2000, Figure 6]. It has been demonstrated that variations in frictional parameters a, b, and L, respectively, across rate- and state-controlled fault models are sufficient to generate nonuniform spatiotemporal evolution of slip [*Liu and Rice*, 2005; *Hillers et al.*, 2006]. Thus some degree of frictional heterogeneity reflecting observed structural properties of fault zones is required to produce irregular slip pattern.

[54] Instead of parameterizing fault zone heterogeneity by variations in frictional properties, we investigated in this study the effects of physically plausible fluid related processes on model seismicity using homogeneous parameter distributions. Although generated slip events show only limited degrees of complexity compared to studies using quenched heterogeneity, our simulations provide insight into possible stopping and nucleation mechanisms. Future studies considering inertia and shear heating are expected to produce more realistic properties of observed seismicity. The present model is a basis for a further study on the influence of pore pressure variation on slip complexity [*Hillers and Miller*, 2006]. The model of *Miller* [2002] clearly demonstrated this influence, but the impact of the inherently discrete model limited these conclusions. Further modeling of observed fluid-related phenomena, such as the migration of pore pressure pulses after large events may generate different seismicity patterns [*Miller et al.*, 2004]. To achieve more realistic response types, subsequent studies will approximate likely heterogeneous distributions of hydraulic diffusivity throughout a fault and vary ε within its physically reasonable limits.

9. Conclusions

[55] We analyzed the effects of hydraulic diffusivity and dilatancy on spatiotemporal evolution of a rate- and state-controlled, fluid-infiltrated extended 2-D fault plane in the continuum limit. The parameter space study of quasi-dynamic simulations reveal that, contrary to the 1-D model by *Segall and Rice* [1995], a transition zone in the undrained limit arises that separates unstable from stable response types. Using the formalism developed by *Segall and Rice* [1995] and *Rice* [1993], we demonstrated that for

Figure 12. Maximum velocities summarizing the response types observed in this study. Grey lines, $f_\eta = 1$; black lines, $f_\eta = 10^4$; dotted line, v^∞. Unstable, seismic stick slip (Figures 12a and 12b), pattern-like, heterogeneous slip evolution with intermittent seismicity, with seismic and aseismic slip rates greater than the loading rate (Figures 12c–12f), sustained oscillations (aseismic) (Figure 12g), and stable creep (Figure 12h). (a) Reference model R1. (b) Reference model R2. (c) Model in transition zone T1, homogeneous properties. (d) Model P1. (e) Model P4. (f) Model P3. (g) Model O2. (h) Arbitrary stable model.

models located in this transition zone the interaction of physically based hydraulic processes on a two-dimensional plane with homogeneous fluid-related properties gives rise to nonuniform spatiotemporal slip pattern. Different degrees of overpressurization, hydraulic diffusivities defining undrained conditions, and dilatancy coefficients from at least half an order of magnitude define a parameter space in which heterogeneous response types are persistent. Although some particular characteristics of the generated nonuniform results such as translational symmetry of slip patterns around $x = X_{\text{length}}/2$ can be assigned to the chosen parameterization, we emphasize that the origin of slip heterogeneity are dilatant hardening processes. As demonstrated, the dilatancy coefficient ε is a crucial parameter controlling the stability of a rate and state friction governed system in the undrained limit, while μ_0 and β are constant. Unfortunately, there has been only a small number of laboratory measurements carried out to determine values for ε. Also, more experiments of coseismically crack-generated porosity are needed. We recognize that the inferred dilatancy coefficient deduced by *Segall and Rice* [1995] from data by *Marone et al.* [1990] is $\varepsilon = 1.7 \times 10^{-4}$, a value too large to generate nonuniform slip pattern in our study, leading only to oscillating response types for a relatively low degree of overpressurization. Drained experiments of *Lockner and Byerlee* [1994] suggest even a somewhat larger value. However, the experiment by *Marone et al.* [1990] was conducted at rather high slip velocities (1–10 μm s^{-1}), implying ε might be significantly smaller at low velocities occurring during the onset of an instability. Hence considering velocity-dependent dilatant effects is expected to support the conclusion drawn here. Nevertheless, further experiments are needed to investigate the potential of dilatant processes to affect the development of slip instabilities.

Notation

t	time.
$\hat{t}$	Interevent time.
Geometry	
x, y, z	coordinates.
X_{length}	length of the fault.
Z_{depth}	depth of the fault.
i, k	along-strike indices.
j, l	downdip indices.
nx/nz	number of cells along strike/depth.
h	cell size.
Time-Dependent Variables	
$\phi(x, z, t)$	porosity.
$v(x, z, t)$	slip velocity.
$\tau(x, z, t)$	shear stress.
$p(x, z, t)$	pore pressure (fault zone).
$\sigma_e(x, z, t)$	effective normal stress.
$\theta(x, z, t)$	state variable.
$u(x, z, t)$	cumulative slip.
$\mu(x, z, t)$	coefficient of friction.
$\tau^r(x, z, t)$	shear stress change.
$\phi_{ss}(x, z, t)$	steady state porosity.
Time-Independent Parameters	
$a(z), b(z)$	frictional parameters.
$\sigma_n(z)$	normal stress.
$p^\infty(z)$	pore pressure (crust).
$p_{\text{hyd}}(z)$	hydrostatic pore pressure.
Parameters (Elastic and Frictional)	
G	rigidity.
v_s	shear wave velocity.
v^∞	plate velocity.
τ^0	background shear stress.
μ_0	nominal friction.
v_0	normalizing constant.
L	critical slip distance.
f_η	damping factor.
K	stiffness matrix.
Parameters (Hydraulic)	
c	hydraulic diffusivity.
L_D	diffusion length scale.
ν	dynamic pore fluid viscosity.
κ	permeability.
m	fluid mass.
β	fluid compressibility.
ε	dilatancy coefficient.
ϕ_0	nominal porosity.
$\tilde{p}$	difference of p to σ_n.
q	specific discharge.
ρ_f	fluid density.
Derived Quantities	
h^*	general critical cell size.
h_u^*	undrained critical cell size.
h_d^*	drained critical cell size.
k^{cr}	general critical stiffness.
k_u^{cr}	undrained critical stiffness.
k_d^{cr}	drained critical stiffness.
$\bar{k}$	normalized critical stiffness.
c^*	effective hydraulic diffusivity.
c_u^*	undrained hydraulic diffusivity.
c_d^*	drained hydraulic diffusivity.
ε_{cr}	critical dilatancy coefficient.
ε^+	maximum ε that makes $h_u^* > 0$.
$\varepsilon_{\tilde{p}}^+$	ε^+ for specific $\tilde{p}$.
λ	overpressurization.
η_0	damping term.
η	effective damping term.
Observed Quantities	
$\Delta\tau$	coseismic shear stress change.
Δu	coseismic slip.
k^{sys}	system stiffness, $\Delta\tau/\Delta u$.

[56] **Acknowledgments.** We thank E. Hairer for numerous comments on handling and improving the stability and performance of the numerical integrator and J. R. Rice and Y. Liu for providing the FFT algorithm for shear stress redistribution. N. Lapusta provided some insightful comments on initial conditions. We thank W. P. Petersen, A. Bongulielmi, T. Racic, D. Schorlemmer, and J. Woessner for computational assistance. We thank two anonymous reviewers whose insightful comments substantially improved this manuscript. The work was sponsored by EC-Project RELIEF (EVG1-CT-2002-00069). This is contribution 1440 of the Institute of Geophysics, ETH Zurich.

References

Andrews, D. J. (2002), A fault constitutive relation accounting for thermal pressurazation of pore fluid, *J. Geophys. Res.*, *107*(B12), 2363, doi:10.1029/2002JB001942.

Bak, P., C. Tang, and K. Wiesenfeld (1987), Self-organized criticality: An explanation of 1/f noise, *Phys. Rev. Lett.*, *59*(4), 381–384.

Beeler, N. M., R. W. Simpson, S. H. Hickman, and D. A. Lockner (2000), Pore fluid pressure, apparent friction, and Coulomb failure, *J. Geophys. Res.*, *105*(B11), 25,533–25,542.

Ben-Zion, Y. (1996), Stress, slip, and earthquakes in models of complex single-fault systems incorporating brittle and creep deformations, *J. Geophys. Res.*, *101*(B3), 5677–5706.

Ben-Zion, Y. (2001), Dynamic rupture in recent models of earthquake faults, *J. Mech. Phys. Solids*, *49*, 2209–2244.

Ben-Zion, Y. (2003), Appendix 2, key formulas in earthquake seismology, in *International Handbook of Earthquake and Engineering Seismology, Part B*, edited by W. H. Lee, H. Kanamori, P. C. Jennings, and C. Kisslinger, pp. 1857–1875, Elsevier, New York.

Ben-Zion, Y., and J. R. Rice (1995), Slip patterns and earthquake populations along different classes of faults in elastic solid, *J. Geophys. Res.*, *100*(B7), 12,959–12,983.

Ben-Zion, Y., and J. R. Rice (1997), Dynamic simulations of slip on a smooth fault in an elastic solid, *J. Geophys. Res.*, *102*(B8), 17,771–17,784.

Blanpied, M. L., D. A. Lockner, and J. D. Byerlee (1991), Fault stability inferred from granite sliding experiments at hydrothermal conditions, *Geophys. Res. Lett.*, *18*(4), 609–612.

Blanpied, M. L., D. A. Lockner, and J. D. Byerlee (1992), An earthquake mechanism based on rapid sealing of faults, *Nature*, *358*, 574–576.

Blanpied, M. L., C. J. Marone, D. A. Lockner, J. D. Byerlee, and D. P. King (1998a), Quantitative measure of the variation in fault rheology due to fluid-rock interactions, *J. Geophys. Res.*, *103*(B5), 9691–9712.

Blanpied, M. L., T. E. Tullis, and J. D. Weeks (1998b), Effects of slip, slip rate, and shear heating on the friction of granite, *J. Geophys. Res.*, *103*(B1), 489–511.

Bosl, W. J., and A. Nur (2002), Aftershocks and pore fluid diffusion following the 1992 Landers earthquake, *J. Geophys. Res.*, *107*(B12), 2366, doi:10.1029/2001JB000155.

Bürgmann, R., S. Ergintav, P. Segall, E. H. Hearn, S. McClusky, R. E. Reilinger, H. Woith, and J. Zschau (2002), Time-dependent distributed afterslip on and deep below the Izmit earthquake rupture, *Bull. Seismol. Soc. Am.*, *92*(1), 126–137.

Burridge, R., and L. Knopoff (1967), Model and theoretical seismicity, *Bull. Seismol. Soc. Am.*, *57*(3), 341–371.

Byerlee, J. (1990), Friction, overpressure and fault normal compression, *Geophys. Res. Lett.*, *17*(12), 2109–2112.

Byerlee, J. (1993), Model for episodic flow of high-pressure water in fault zones before earthquakes, *Geology*, *21*, 303–306.

Caine, J. S., J. P. Evans, and C. B. Forster (1996), Fault zone architecture and permeability structure, *Geology*, *24*, 1025–1028.

Carlson, J. M., and J. S. Langer (1989), Mechanical model of an earthquake fault, *Phys. Rev. A*, *40*(11), 6470–6484.

Chambon, G., and J. W. Rudnicki (2001), Effects of normal stress variations on frictional stability of a fluid-infiltrated fault, *J. Geophys. Res.*, *106*(B6), 11,353–11,372.

Chinnery, M. (1963), The stress changes that accompany strike-slip faulting, *Bull. Seismol. Soc. Am.*, *53*, 921–932.

Cocco, M., and J. R. Rice (2002), Pore pressure and poroelasticity effects in Coulomb stress analysis of earthquake interactions, *J. Geophys. Res.*, *107*(B2), 2030, doi:10.1029/2000JB000138.

Cochard, A., and R. Madariaga (1996), Complexity of seismicity due to highly rate-dependent friction, *J. Geophys. Res.*, *105*(B11), 25,891–25,907.

Cox, S. F. (1995), Faulting processes at high fluid pressures: An example of fault valve behavior from the Wattle Gully Fault, Victoria, Australia, *J. Geophys. Res.*, *100*(B7), 12,841–12,859.

David, C., T.-F. Wong, W. Zhu, and J. Zhang (1994), Laboratory measurement of compaction-induced permeability change in porous rocks: Implications for the generation and maintenance of pore pressure excess in the crust, *Pure Appl. Geophys.*, *143*, 425–456.

Dieterich, J. H. (1979), Modeling of rock friction: 1. Experimental results and constitutive equations, *J. Geophys. Res.*, *84*(B5), 2161–2168.

Dieterich, J. H. (1992), Earthquake nucleation on faults with rate- and state-dependent strength, *Tectonophysics*, *211*, 115–134.

Faulkner, D. R., and E. H. Rutter (2001), Can the maintenance of overpressured fluids in large strike-slip faults zones explain their apparent weakness?, *Geology*, *29*, 503–506.

Fisher, A., and G. Zwart (1996), Relation between permeability and effective stress along a plate-boundary fault, Barbados accretionary complex, *Geology*, *24*, 307–310.

Fitzenz, D. D., and S. A. Miller (2001), A forward model for earthquake generation on interacting faults including tectonics, fluids, and stress transfer, *J. Geophys. Res.*, *106*(B11), 26,689–26,706.

Garagash, D. I., and J. W. Rudnicki (2003a), Shear heating of a fluid-saturated slip-weakening dilatant fault zone: 1. limiting regimes, *J. Geophys. Res.*, *108*(B2), 2121, doi:10.1029/2001JB001653.

Garagash, D. I., and J. W. Rudnicki (2003b), Shear heating of a fluid-saturated slip-weakening dilatant fault zone: 2. quasi-drained regime, *J. Geophys. Res.*, *108*(B10), 2472, doi:10.1029/2002JB002218.

Gu, J.-C., J. R. Rice, A. L. Ruina, and S. T. Tse (1984), Slip motion and stability of a single degree of freedom elastic system with rate and state dependent friction, *J. Mech. Phys. Solids*, *32*, 167–196.

Hairer, E., and G. Wanner (Eds.) (1996), *Solving Ordinary Differential Equations II. Stiff and Differential-Algebraic Problems*, 2nd ed., 614 pp., Springer, New York.

Hearn, E. H., and R. B. R. E. Reilinger (2002), Dynamics of Izmit earthquake postseismic deformation and loading of the Düzce earthquake hypocenter, *Bull. Seismol. Soc. Am.*, *92*(1), 172–193.

Hill, D. P., et al. (1993), Seismicity remotely triggered by the magnitude 7.3 Landers, California, earthquake, *Science*, *260*, 1617–1623.

Hillers, G. (2006), On the origin of earthquake complexity in continuum fault models with rate and state friction, Ph.D. thesis, Swiss Fed. Inst. of Technol., Zurich. (Available at http://hdl.handle.net/2122/1024)

Hillers, G., and S. A. Miller (2006), Dilatancy controlled spatio-temporal slip evolution of a sealed fault with spatial variations of the pore pressure, *Geophys. J. Int.*, in press.

Hillers, G., Y. Ben-Zion, and P. M. Mai (2006), Seismicity on a fault with rate- and state-dependent friction and spatial variations of the critical slip distance, *J. Geophys. Res.*, *111*, B01403, doi:10.1029/2005JB003859.

Hirose, H., and K. Hirahara (2002), A model for complex slip behavior on a large asperity at subduction zones, *Geophys. Res. Lett.*, *29*(22), 2068, doi:10.1029/2002GL015825.

Husen, S., R. Taylor, R. B. Smith, and H. Healser (2004), Changes in geyser eruption behavior and remotely triggered seismicity in Yellowstone National Park produced by the 2002 *M* 7.9 Denali fault earthquake, Alaska, *Geology*, *32*, 537–540.

Ito, K., and M. Matsuzaki (1990), Earthquakes as self-organized critical phenomena, *J. Geophys. Res.*, *95*(B5), 6853–6860.

Kato, N., and T. Hirasawa (1997), A numerical study on seismic coupling along subduction zones using a laboratory-derived friction law, *Phys. Earth Planet. Inter.*, *102*, 51–68.

Kato, N., and T. Hirasawa (1999), Nonuniform and unsteady sliding of a plate boundary in a great earthquake cycle: A Numerical simulation using a laboratory-derived friction law, *Pure Appl. Geophys.*, *155*, 93–118.

Langer, J. S., J. M. Carlson, C. R. Myers, and B. E. Shaw (1996), Slip complexity in dynamic models of earthquake faults, *Proc. Natl. Acad. Sci. U.S.A.*, *93*, 3825–3829.

Lapusta, N., and J. R. Rice (2003), Nucleation and early seismic propagation of small and large events in a crustal earthquake model, *J. Geophys. Res.*, *108*(B4), 2205, doi:10.1029/2001JB000793.

Lapusta, N., J. R. Rice, Y. Ben-Zion, and G. Zheng (2000), Elastodynamic analysis for slow tectonic loading with spontaneous rupture episodes on faults with rate- and state-dependent friction, *J. Geophys. Res.*, *105*(B10), 23,765–23,789.

Liu, Y., and J. R. Rice (2005), Aseismic slip transients emerge spontaneously in three-dimensional rate and state modeling of subduction earthquake sequences, *J. Geophys. Res.*, *110*, B08307, doi:10.1029/2004JB003424.

Lockner, D. A., and J. D. Byerlee (1994), Dilatancy in hydraulically isolated faults and the suppression of instability, *Geophys. Res. Lett.*, *21*(22), 2353–2356.

Lockner, D. A., and J. D. Byerlee (1995), An earthquake instability model based on faults containing high fluid-pressure compartments, *Pure Appl. Geophys.*, *145*, 717–745.

Lomnitz-Adler, J. (1993), Automaton models of seismic fracture: Constraints imposed by the magnitude-frequency relation, *J. Geophys. Res.*, *98*(B10), 17,745–17,756.

Marone, C., C. B. Rayleigh, and C. H. Scholz (1990), Frictional behavior and constitutive modeling of simulated fault gouge, *J. Geophys. Res.*, *95*(B5), 7007–7025.

Miller, S. A. (2002), Properties of large ruptures and the dynamical influence of fluids on earthquakes and faulting, *J. Geophys. Res.*, *107*(B9), 2182, doi:10.1029/2000JB000032.

Miller, S. A., A. Nur, and D. L. Olgaard (1996), Earthquakes as a coupled shear stress-high pore pressure dynamical system, *Geophys. Res. Lett.*, *23*(2), 197–200.

Miller, S. A., Y. Ben-Zion, and J.-P. Burg (1999), A three-dimensional fluid-controlled earthquake model: Behavior and implications, *J. Geophys. Res.*, *104*(B5), 10,621–10,638.

Miller, S. A., C. Collettini, L. Chiaraluce, M. Cocco, M. Barchi, and J. P. Kaus (2004), Aftershocks driven by a high-pressure CO_2 source at depth, *Nature*, *427*, 724–727.

Miyazaki, S., P. Segall, J. Fukuda, and T. Kato (2004), Space time distribution of afterslip following the 2003 Tokachi-oki earthquake: Implications for variations in fault zone frictional properties, *Geophys. Res. Lett.*, *31*, L06623, doi:10.1029/2003GL019410.

Moore, J. C. (1995), Abnormal fluid pressures and fault-zone dilation in the Barbados accretionary prism: Evidence from logging while drilling, *Geology*, *23*, 605–608.

Moore, J. C., D. A. Lockner, and J. D. Byerlee (1994), Reduction of permeability in granite at elevated temperatures, *Science*, *265*, 1558–1561.

Nielsen, S. B., J. M. Carlson, and K. B. Olsen (2000), Influence of friction and fault geometry on earthquake rupture, *J. Geophys. Res.*, *105*(B3), 6069–6088.

Nur, A., and J. R. Booker (1972), Aftershocks caused by pore fluid flow?, *Science*, *175*, 885–887.

Nur, A., and J. Walder (1992), Hydraulic pulses in the Earth's crust, in *Fault Mechanics and Transport Properties in Rocks*, edited by B. Evans and T.-F. Wong, pp. 459–473, Elsevier, New York.

Piombo, A., G. Martinelli, and M. Dragoni (2005), Post-seismic fluid flow and Coulomb stress changes in a poroelastic medium, *Geophys. J. Int.*, *162*, 507–515.

Rice, J. R. (1992), Fault stress states, pore pressure distributions, and the weakness of the San Andreas Fault, in *Fault Mechanics and Transport Properties in Rocks*, edited by B. Evans and T.-F. Wong, pp. 475–503, Elsevier, New York.

Rice, J. R. (1993), Spatiotemporal complexity of slip on a fault, *J. Geophys. Res.*, *98*(B6), 9885–9907.

Rice, J. R., and Y. Ben-Zion (1996), Slip complexity in earthquake fault models, *Proc. Natl. Acad. Sci. U.S.A.*, *93*, 3811–3818.

Rice, J. R., and A. L. Ruina (1983), Stability of steady frictional slipping, *J. Appl. Mech.*, *50*, 343–349.

Rubin, A. M., and J.-P. Ampuero (2005), Earthquake nucleation on (aging) rate and state faults, *J. Geophys. Res.*, *110*, B11312, 2410, doi:10.1029/2005JB003686.

Rudnicki, J. W., and C.-H. Chen (1988), Stabilization of rapid frictional slip on a weakening fault by dilatant hardening, *J. Geophys. Res.*, *93*(B5), 4745–4757.

Ruina, A. (1983), Slip instability and state variable friction laws, *J. Geophys. Res.*, *88*(B12), 10,359–10,370.

Segall, P. (1996), Earthquakes: Slow down for safety, *Nature*, *383*, 21–22.

Segall, P., and J. R. Rice (1995), Dilatancy, compaction, and slip instability of a fluid-infiltrated fault, *J. Geophys. Res.*, *100*(B11), 22,155–22,171.

Shaw, B. E., and J. R. Rice (2000), Existence of continuum complexity in the elastodynamics of repeated fault ruptures, *J. Geophys. Res.*, *105*(B10), 23,791–23,810.

Shibazaki, B., and Y. Iio (2003), On the physical mechanism of silent slip events along the deeper part of the seismogenic zone, *Geophys. Res. Lett.*, *30*(9), 1489, doi:10.1029/2003GL017047.

Sibson, R. H. (1992), Implications of fault-valve behavior for rupture nucleation and recurrence, *Tectonophysics*, *211*, 283–293.

Sibson, R. H. (1994), Crustal stress, faulting and fluid flow, in *Geofluids: Origin, Migration and Evolution of Fluids in Sedimentary Basins*, edited by J. Parnell, *Geol. Soc. Spec. Publ.*, *78*, 69–84.

Sibson, R. H., and J. V. Rowland (2003), Stress, fluid pressure and structural permeability in seismogenic crust, North Island, New Zealand, *Geophys. J. Int.*, *154*, 584–594.

Sleep, N. H. (1995), Ductile creep, compaction, and rate and state dependent friction within major fault zones, *J. Geophys. Res.*, *100*(B7), 13,065–13,080.

Sleep, N. H. (1997), Application of a unified rate and state friction theory to the mechanics of fault zones with strain localization, *J. Geophys. Res.*, *102*(B2), 2875–2895.

Sleep, N. H., and M. L. Blanpied (1992), Creep, compaction and the weak rheology of major faults, *Nature*, *359*, 687–692.

Stuart, W. D., and T. E. Tullis (1995), Fault model for preseismic deformation at Parkfield, California, *J. Geophys. Res.*, *100*(B12), 24,079–24,099.

Taylor, M. A. J., and J. R. Rice (1998), Dilatant stabilization of subduction earthquake rupture into the shallow thrust interface, *Eos Trans. AGU*, *79*(45), Fall Meet. Suppl., F631.

Tse, S. T., and J. R. Rice (1986), Crustal earthquake instability in relation to the depth variation of frictional slip properties, *J. Geophys. Res.*, *91*(B9), 9452–9472.

Waite, G. P., and R. B. Smith (2002), Seismic evidence for fluid migration accompanying subsidence of the Yellowstone caldera, *J. Geophys. Res.*, *107*(B9), 2177, doi:10.1029/2001JB000586.

Walder, J., and A. Nur (1984), Porosity reduction and pore pressure development, *J. Geophys. Res.*, *89*(B13), 11,539–11,548.

Wibberly, C. A. J., and T. Shimamoto (2003), Internal structure and permeability of major strike-slip fault zones: The Median Tectonic Line in Mie Prefecture, southwest Japan, *J. Struct. Geol.*, *25*, 59–78.

Yamashita, T. (1998), Simulation of seismicity due to fluid migration in fault zone, *Geophys. J. Int.*, *132*, 674–686.

Zhang, S., and T. E. Tullis (1998), The effect of fault slip on permeability and permeability anisotropy in quartz gouge, *Tectonophysics*, *295*, 41–52.

Zhang, S., T. E. Tullis, and V. J. Scruggs (1999), Permeability anisotropy and pressure dependency of permeability in experimentally sheared gouge materials, *J. Struct. Geol.*, *21*, 795–806.

Zhang, S., T. E. Tullis, and V. J. Scruggs (2001), Implications of permeability and its anisotropy in a mica gouge for pore pressure in fault zones, *Tectonophysics*, *335*, 37–50.

Zhao, D., D. Kanamori, H. Negishi, and D. Wiens (1996), Tomography of the source area of the 1995 Kobe earthquake: Evidence for fluids at the hypocenter?, *Science*, *274*, 1891–1894.

Zöller, G., S. Hainzl, M. Hohlschneider, and Y. Ben-Zion (2005), Aftershocks resulting from creeping sections in a heterogeneous fault, *Geophys. Res. Lett.*, *32*, L03308, doi:10.1029/2004GL021871.

G. Hillers, Institute for Crustal Studies, University of California, Santa Barbara, CA 93106-1100, USA. (gregor@crustal.ucsb.edu)

S. A. Miller, Department of Geodynamics and Geophysics, University of Bonn, Nussallee 8, D-53115 Bonn, Germany.